Diapycnal mixing and tracer dispersion in a terrain-following coordinate model

Noémie Schifano[1], Clément Vic[1], Jonathan Gula[1,2,3], M. Jeroen Molemaker[3], James C. McWilliams[3]

[1]Univ Brest, CNRS, Ifremer, IRD, Laboratoire d'Océanographie Physique et Spatiale (LOPS), IUEM, Plouzané, France
[2]Institut Universitaire de France (IUF), Paris, France
[3]Department of Atmospheric and Oceanic Sciences and Institute of Geophysics and Planetary Physics, University of California, Los Angeles, CA 90095-1565, United States

Key Points:

- Effective diapycnal mixing is quantified in realistic high-resolution simulations using passive tracer experiments and online buoyancy diagnostics
- Effective diapycnal mixing is close to parameterized values over the abyssal plain but can be larger above steep ridge slopes
- Numerical mixing is minimized by smoothing topography and effective mixing aligns closely with parameterized mixing

Corresponding author: N. Schifano, `noemie.schifano@univ-brest.fr`

Abstract

Diapycnal mixing, driven by small-scale turbulence, is crucial for the global ocean circulation, particularly for the upwelling of deep water masses. However, accurately representing diapycnal mixing in ocean models is challenging because numerical errors can introduce significant numerical mixing. In this study, we explore the diapycnal mixing in a high-resolution regional model of the North Atlantic subpolar gyre using the Coastal and Regional Ocean Community model (CROCO). CROCO uses terrain-following vertical coordinates that do not align with isopycnals. As such, tracer advection schemes produce spurious diapycnal mixing, which can nonetheless be reduced using rotated advection schemes. We focus on how different advection schemes and vertical resolutions affect numerical diapycnal mixing. Our approach includes online diagnostics of buoyancy fluxes and tracer release experiments to quantify the effective mixing, which combines parameterized and numerical diapycnal mixing. Our main results show that in flat-bottom regions, the effective diapycnal mixing is close to the parameterized mixing. However, in regions with steep topography, numerical mixing can locally significantly exceed parameterized mixing due to grid slope constraints imposed by the rotated mixing operator. While topography smoothing can mitigate this excessive mixing, it can also alter flow-topography interactions. In addition, while a higher vertical resolution reduces the numerical mixing induced by the vertical tracer advection, it can also increase numerical mixing in steep regions by introducing a stronger constraint on the grid slope. These results underscore that diapycnal mixing representation in a numerical model requires balancing high resolution and topographic smoothing with the control of numerical errors.

Plain Language Summary

The mixing of waters of different densities is a key physical phenomenon that enables deep water to rise gradually to the surface. However, our knowledge of mixing is limited, so numerical models that realistically reproduce the physics of the oceans are essential tools. Nevertheless, the implementation of mixing in numerical models is not necessarily under control. We used a realistic configuration of the North Atlantic Ridge based on the CROCO numerical model. We compared several numerical and mathematical parameters. Our results show that, over a flat bottom, mixing is under control with a vertical resolution of 25 metres. However, over steep slopes, numerical limits are imposed that generate mixing which is sometimes a hundred times stronger than the mixing explicitly parameterised in the model. To control mixing independently of seafloor shape, we smoothed the seafloor topography beyond common practice, thereby losing realism. Therefore, representing the important phenomenon of mixing between waters of different densities involves a trade-off between a good representation of reality and numerical difficulties.

1 Introduction

The low-frequency and large-scale ocean circulation is mostly adiabatic, as water masses move predominantly along surfaces of constant density, or isopycnals. However, diabatic processes, which involve mixing across isopycnals, are crucial for closing the general circulation (de Lavergne et al., 2022). This diapycnal mixing shapes the lower limb of the meridional overturning circulation (e.g., Stommel, 1958; Samelson & Vallis, 1997). Recent theories of the abyssal circulation insist on the role of diapycnal mixing, and its still partially uncovered space and time variability, in the upwelling of the heaviest water masses (e.g., reviewed in de Lavergne et al., 2022).

Yet, diapycnal mixing remains difficult to map globally and statistically, because its main driver is small-scale turbulence, which is patchy and intermittent by nature. The most accurate estimate of diapycnal mixing is obtained by microstructure (very high frequency) measurements of velocity shear (a review of the measurement techniques can be found in Frajka-Williams et al., 2022). Indirect techniques for measuring diapycnal mixing, such as Tracer Release Experiments (TRE), have been developed to assess the intensity of mixing over different time and space scales (Ledwell & Watson, 1991). Direct and indirect measurements have revealed the very large variability of diapycnal mixing throughout the world's oceans (Ledwell et al., 1993, 2000; Naveira Garabato et al., 2004; Kunze et al., 2006; Waterhouse et al., 2014).

The main energy sources for diapycnal mixing are tides and winds (Munk & Wunsch, 1998). They generate internal gravity waves that travel through the ocean before breaking, triggering diapycnal mixing (see Whalen et al. (2020) for a recent review). Topographic wakes and associated submesoscale instabilities can also be a strong source of interior diapycnal mixing (Gula et al., 2016; Naveira Garabato et al., 2019; Mashayek et al., 2024). In situ measurements have shown that the magnitude of diapycnal mixing varies by several orders of magnitude heavily depending on the underlying seafloor topography (see, for example, Figure 7 in Waterhouse et al. (2014)).

Successive refinements in the knowledge of the physics and energetics of internal waves have led to the development of parameterizations of diapycnal mixing driven by internal waves for global ocean circulation models that will not resolve them in a foreseeable future (e.g., Jayne & St Laurent, 2001; Olbers & Eden, 2013; de Lavergne et al., 2019, 2020; Alford, 2020). In primitive-equation regional and global models that include tidal forcing and high-frequency atmospheric forcing, internal gravity waves and other small-scale instability processes that lead to diapycnal mixing can be partially represented (e.g., Zilberman et al., 2009; Arbic et al., 2010; Gula et al., 2016; Vic et al., 2018; Mazloff et al., 2020; Thakur et al., 2022). As a result, specific parameterizations for diapycnal mixing driven by internal waves are not typically employed. Instead, diapycnal mixing is parameterized using turbulent closures that bridge the gap between internal waves, small-scale instability processes, and actual mixing. For example, the K-profile parameterization (KPP, Large et al., 1994), one of the most widely used schemes for parameterizing diffusivity in the boundary layers, is typically extended with distinct parameterizations to represent processes in the ocean interior, such as shear instability and internal wave activity. In the interior, it assumes that the resolved velocity field generates sufficient vertical shear to trigger Richardson-number-based mixing, while a background diffusivity is prescribed to account for the effects of internal wave breaking not captured by the model.

In addition to the parameterized mixing, advection schemes produce additional mixing, often undesired, sometimes called 'numerical' or 'spurious' mixing (Griffies et al., 1998, 2000; Lee et al., 2002; Hofmann & Morales Maqueda, 2006; Burchard & Rennau, 2008; Marchesiello et al., 2009; Hecht, 2010; Hill et al., 2012; Bracco et al., 2018; Megann, 2018; Klingbeil et al., 2019). This numerical mixing is an important issue because it includes a diapycnal component that potentially exceeds the parameterized mixing, sometimes by several orders of magnitude (Bracco et al., 2018). Its intensity is determined by the accuracy of the advection schemes, the horizontal and vertical resolution, and the nature of the coordinate system (geopotential, isopycnal, or terrain-following coordinates). Strategies have been designed to minimise the diapycnal part of the numerical mixing by rotating it along isoneutral surfaces (Griffies et al., 1998), with solutions specifically designed for terrain-following coordinates (Marchesiello et al., 2009; Lemarié et al., 2012a). However, the impact of such solutions on the effective diapycnal mixing, defined as the sum of parameterized and numerical mixing, has rarely been quantified for regional submesoscale-permitting or submesoscale-resolving models, especially in the presence of tides and other high-frequency motions. If one wants to use a primitive-equation model specifically to study diabatic processes, and their impact on water mass transformation and deep ocean circulation, they cannot ignore mixing due to advection schemes.

Several methods have been developed to diagnose numerical mixing in ocean models. Historical methods are based on the water mass transformation framework (e.g., Lee et al., 2002; Megann, 2018). Other indirect methods are based on the evaluation of long-term changes in variables directly related to diapycnal mixing (e.g. available potential energy, Griffies et al., 2000; Ilıcak et al., 2012). More direct methods, i.e. those that provide local estimates of mixing in space and time, are based on passive tracer diapycnal spreading (e.g., in z-level models, Getzlaff et al., 2010, 2012) or tracer variance decay (mostly in coastal environments, Burchard & Rennau, 2008; Burchard et al., 2008; Klingbeil et al., 2014; Burchard et al., 2021; Banerjee et al., 2024). The latter has the advantage of providing a more local estimate, although it cannot directly separate isopycnal from diapycnal fluxes. Thus, it is still difficult to obtain local estimates in time and space for diapycnal buoyancy fluxes and associated diapycnal diffusivities, and we propose here a method to provide such an estimate.

In the present study, we aim to quantify the spurious diapycnal mixing due to different tracer advection schemes routinely used in the Coastal and Regional Ocean Community model (CROCO), based on the Regional Oceanic Modelling System (ROMS, Shchepetkin & McWilliams, 2005). We pay particular attention to how the advection schemes, in combination with different vertical resolutions, affect the representation of passive tracers.

To tackle these numerical questions, we set up a regional configuration in the subpolar North Atlantic, which includes part of the Reykjanes Ridge and the Iceland Basin. This region is of particular interest because it is located at the gateway of dense water formation (Piron et al., 2017) and has several sources of turbulence due to strong wind events and flow-topography interactions (Vic et al., 2021). It has also received particular attention from the modeling community due to the challenge of accurately modeling the Nordic deep overflows (e.g., Bruciaferri et al., 2024). We use microstructure measurements from three cruises to provide an order of magnitude estimate of the actual mixing rates against which the mixing parameterisation used in the model can be compared. The numerical mixing is estimated using a novel ad hoc online diagnostic based on the direct computation of buoyancy fluxes in the diapycnal direction, and passive tracer release experiments (TREs). While the former allows us to estimate the pointwise extra mixing due to the numerical schemes, the latter are a useful tool to visually capture the specific features of each scheme, and also to independently quantify the amount of mixing experienced by a tracer over different physical and numerical conditions (as highlighted in Getzlaff et al., 2012). We also argue that the tracers can be seen as localized patches of biological or geochemical material to illustrate how the tracers' behavior is affected by numerical choices.

In section 2, we present the model configuration and the set of simulations we designed to investigate the impact of numerical choices on diapycnal mixing. We also present the different methods used to quantify diapycnal mixing, online, and based on the TREs. In section 3, we present an overview of the simulated dynamics along with a comparison of the simulated mixing with in situ estimates from microstructure data. We then compare the different estimates of diapycnal mixing (parameterized vs diagnosed following the different methods) in different regions, over smooth vs steep and rough topography. The impact of the advection schemes on the tracer representation is illustrated. In section 4 we summarize the results and discuss the limitations of the methods as well as the implications of our findings.

2 Methods

2.1 Numerical set up

We perform three-dimensional realistic simulations using the ocean model CROCO (Auclair et al., 2022). CROCO has been developed on the basis of ROMS (Shchepetkin & McWilliams, 2005) and still shares a significant amount of code, in particular most of the numerical options detailed below. It solves the primitive equations and uses horizontal orthogonal curvilinear coordinates (ξ, η) and vertical terrain-following coordinates, usually called σ-levels when unstretched and s-levels when surface and bottom stretching is used. We use s-levels with standard CROCO/ROMS surface and bottom stretching parameters $\theta_s = 5$, $\theta_b = 2$ and $h_c = 300$ m (depth above which levels come closer together). We use the hydrostatic version of the code. The model domain covers part of the Reykjanes Ridge, south of Iceland, and part of the Iceland Basin to its east (Figure 1). The model grid has 1000×800 points in the horizontal with a grid spacing of 800 m. The number of vertical levels varies between 50 and 200 across the set of simulations (Section 2.2 and Table 1). The horizontal resolution is among the standards in the regional modelling community (e.g., Thakur et al., 2022; Delpech et al., 2024), and allows to resolve the mesoscales and partially resolve the submesoscales and the internal gravity wave continuum (e.g., Arbic, 2022). CROCO uses a split-explicit time-stepping for the free surface and a third-order predictor-corrector scheme (referred to as LFAM3) for tracers and baroclinic momentum (Shchepetkin & McWilliams, 2005). All simulations are run with a baroclinic time step of 80 seconds and 50 barotropic time steps between two consecutive baroclinic time steps.

The model bathymetry is based on the 15-second resolution Shuttle Radar Topography Mission dataset (SRTM15_PLUS, Tozer et al., 2019). The raw bathymetry is smoothed with a Gaussian kernel with a radius of 5 grid points to avoid steep gradients that could lead to pressure gradient errors (Shchepetkin & McWilliams, 2003). A steepness parameter (also known as slope parameter) can be defined as $rx_0 = |\delta h|/2\overline{h}$, where $\overline{h}$ is the bottom depth averaged over adjacent cells and δh is the horizontal change in h for adjacent cells (Beckmann & Haidvogel, 1993a). Here, rx_0 does not exceed 0.062 (Fig. A1), which is well below the typically recommended threshold of 0.2 (Lemarié et al., 2012a; Debreu et al., 2020). It is also in the range of the more restrictive values recommended in more recent studies (Wise et al., 2022; Bruciaferri et al., 2024). A more detailed evaluation of the impact of pressure gradient errors in our configurations can be found in Appendix A.

Atmospheric forcing is provided at hourly resolution by the Climate Forecast System Reanalysis (CFSR, Saha et al., 2010). Initial and boundary conditions are provided by a parent simulation covering the entire Atlantic Ocean at 3-km resolution, GIGATL3 (Gula et al., 2021). The parent simulation includes barotropic and baroclinic tides. Thus, the tidal forcing is embedded in the boundary conditions at hourly resolution. We initialize the simulations in Aug 2008 and run them for 2 months, with a spin-up of 10 days. The setup has much in common with the configurations of Le Corre et al. (2020) and Barkan et al. (2021a). The realism of the large-scale circulation was assessed in Le Corre et al. (2020), while the modelled currents and kinetic energy spectra were validated against observations from moored current meters in Barkan et al. (2021a).

All simulations presented below employ the third-order upwind scheme (UP3) for horizontal momentum advection (Shchepetkin & McWilliams, 2005). This scheme introduces an implicit diffusion term that acts as hyperdiffusion, with a coefficient proportional to the local velocity: $B = \frac{1}{12}\,|U|\,\Delta^3$, where U is the local velocity and Δ the horizontal grid spacing (Marchesiello et al., 2009). Momentum advection can contribute to numerical diapycnal mixing (e.g., Ilıcak et al., 2012; Megann & Storkey, 2021), which can be assessed using the grid Reynolds number Re_Δ, defined as the ratio of advective to viscous forces. Assuming a biharmonic viscosity B, the grid Reynolds number is: $Re =$

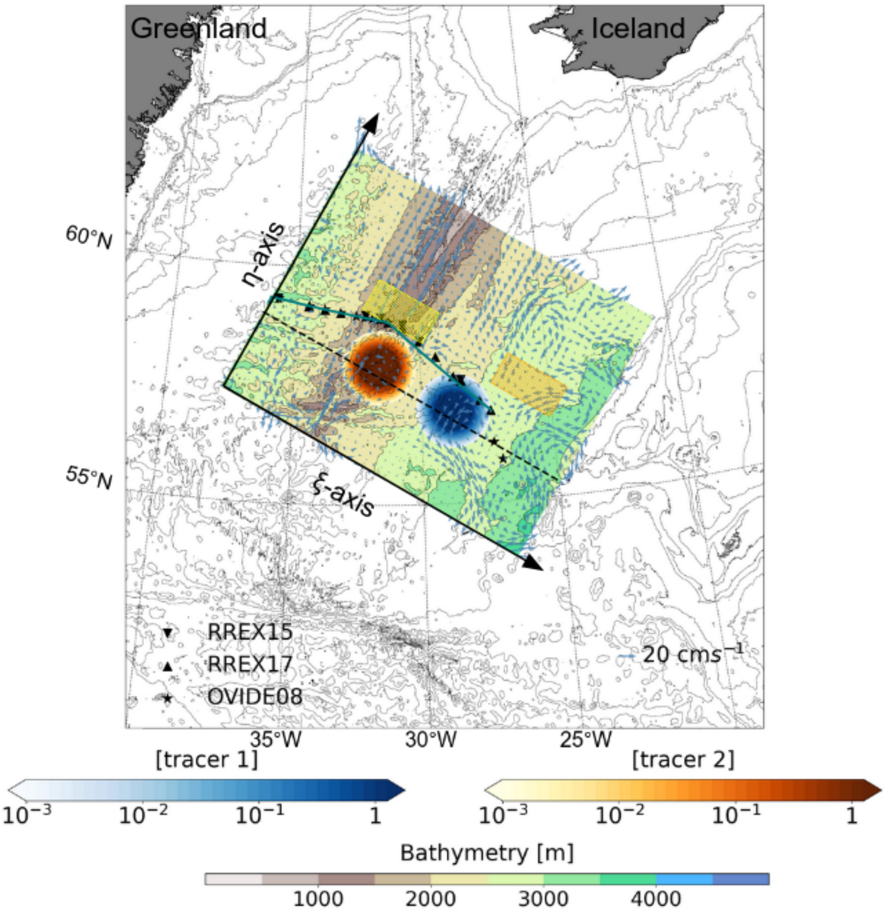

Figure 1. Model domain and bathymetry. Red and blue colorbars indicate the release of passive tracer patches. Tracer patch 1 is released at ρ= 1027.700 kg m^{-3}, while tracer patch 2 is released at ρ= 1027.775 kg m^{-3}. Tracer concentrations are summed over depth. The arrows represent the time-averaged circulation at 1000 meters depth (approximate depth of tracer release) over 40 days. The yellow and orange dashed areas are used to contrast the mixing profiles between the ridge and the abyssal plain in section 3.1. The black dashed line is the vertical section used in figures 4, 5 and 8; the purple area represents the width of the section used in figures 10 and 12. The pictograms represent the location of in situ measurements of energy dissipation from different cruises (see legend). The gray line is the vertical section used to plot model diffusivities in figure 6. Bathymetry is from SRTM15_PLUS (Tozer et al., 2019).

$\frac{|U|\Delta^3}{B}$ (Griffies & Hallberg, 2000). For the UP3 scheme used here, this yields $Re_\Delta = 12$, which remains below the stability threshold for biharmonic viscosity ($Re_\Delta < 16$) derived by Griffies and Hallberg (2000). Thus, by its design, this horizontal momentum advection scheme maintains a low grid Reynolds number, ensuring numerical stability (Marchesiello et al., 2009; Soufflet et al., 2016). Furthermore, empirical evidence found that this scheme leads to relatively low spurious mixing when compared to comparative explicit viscosities (Ilıcak et al., 2012).

Horizontal advection schemes for active tracers (potential temperature and salinity) are third-order upwind scheme (UP3), split and rotated upstream biased schemes of the third (RSUP3) or fifth order (RSUP5) depending on the experiments. The latter two are modified versions of upwind schemes, in which the diffusive part is rotated along isoneutral surfaces (details on the split and rotation methods are given in Marchesiello et al., 2009; Lemarié et al., 2012a). This modification of the upstream schemes was designed to limit the spurious diapycnal mixing inherent to the non-alignment of s-coordinate surfaces with isopycnals. However, there are constraints on the maximum values of the isopycnal slope α_m and the grid slope ratio s_m for which the diffusive part of the advection schemes can be rotated along isopycnals:

$$\alpha_m = \max\left(\frac{\partial \rho}{\partial \xi}\Big/\frac{\partial \rho}{\partial z}, \frac{\partial \rho}{\partial \eta}\Big/\frac{\partial \rho}{\partial z}\right) < \alpha_c = 0.05, \tag{1}$$

$$s_m = \max\left(\frac{\Delta_\xi}{\Delta_z}\frac{\partial \rho}{\partial \xi}\Big/\frac{\partial \rho}{\partial z}, \frac{\Delta_\eta}{\Delta_z}\frac{\partial \rho}{\partial \eta}\Big/\frac{\partial \rho}{\partial z}\right) < s_c = 1, \tag{2}$$

where Δ_i represents the distance between neighboring grid points in the i direction (along the sloping model layers for the horizontal directions). These limits ensure the stability of the code, as discussed in Marchesiello et al. (2009) and Lemarié et al. (2012b). But at locations where $\alpha_m > \alpha_c$ or $s_m > s_c$, the diffusion will be along the directions defined by the critical slopes α_c or s_c, and thus not strictly aligned with the isopycnals (Marchesiello et al., 2009; Lemarié et al., 2012a). Note that a time filter can be added to the isoneutral slope calculation to limit possible numerical instabilities due to the nonlinearity of the equation of state in certain regimes (Griffies et al., 1998). This was not used in the experiments presented here, but an experiment including the time filter is provided in Appendix B.

The vertical advection of momentum and active tracers uses a fourth-order centered parabolic spline reconstruction (SPLINES), with an adaptive, Courant-number-dependent implicit scheme (Shchepetkin, 2015).

The advection of passive tracers uses either the same schemes as for active tracers (RSUP3 or RSUP5 in the horizontal, and SPLINES in the vertical) or a 5th-order Weighted Essentially Non-Oscillatory scheme (WENO5, Jiang & Shu, 1996) in all directions. The WENO5 scheme is a common choice for biogeochemical tracers, mainly because it limits negative concentration for tracers. Therefore, it is important to assess how it affects numerical mixing as it would affect the global cycles of biogeochemical tracers. The different combinations of schemes for our sensitivity studies are summarized in Table 1.

The subgrid scale vertical mixing is parameterised using the KPP scheme (Large et al., 1994). KPP is a closure for scalar and momentum turbulent fluxes that provides the vertical eddy diffusivity coefficient K_{KPP}. In the surface and bottom layers, which are calculated based on a critical bulk Richardson number, K_{KPP} is the product of the boundary layer thickness h_{bl}, a turbulent velocity scale w_S and a shape function G, both of which depend on the vertical coordinate s:

$$K_{KPP} = h_{bl} w_S(s) G(s). \tag{3}$$

In the interior, outside these layers, K_{KPP} is calculated as the sum of three processes: Background internal wave breaking, vertical shear instability, and convective instability. Background internal wave breaking is parameterized with a constant background diffusivity ($K^w = 10^{-5}$ m^2 s^{-1} for tracers). Vertical shear instability is parameterized using the Richardson number $Ri = N^2/S^2$, where N^2 is the buoyancy frequency squared and $S^2 = \left(\frac{\partial u}{\partial z}\right)^2 + \left(\frac{\partial v}{\partial z}\right)^2$ is the squared vertical shear of the horizontal velocity, using the same formulation as in Large et al. (1994):

$$K^S = \begin{cases} \nu^0 & Ri < 0 \\ \nu^0 \left[1 - \left(\frac{Ri}{Ri_c}\right)^2\right]^3 & 0 < Ri < Ri_c \\ 0 & Ri_c < Ri \end{cases} \tag{4}$$

with a critical Richardson number $Ri_c = 0.7$ and $\nu^0 = 5 \times 10^{-3}$ m^2 s^{-1}. In case of convective instability ($N^2 \leq 0$), an additional diffusivity $K^C = 10^{-1}$ m^2 s^{-1} is added. Note that there is no subgrid scale lateral mixing operator for momentum and tracers, as there is enough implicit mixing provided by the advection schemes (Shchepetkin & McWilliams, 1998).

2.2 Set of simulations

We focus here on two aspects that affect numerical mixing: the vertical resolution and the advective schemes. With terrain-following levels, the local vertical resolution depends on the number of model levels (s-levels) and the local depth (Figure 2). We tested the sensitivity of numerical diapycnal mixing to the vertical resolution comparing simulations with 50, 100 and 200 vertical levels. While the use of 50 levels (or less) has long been in the range of the community standards (e.g., Marchesiello et al., 2003; Penven et al., 2005), the use of ≈100 levels has become routine to better represent current-topography interactions (e.g., Molemaker et al., 2015; Gula et al., 2016, 2019; Vic et al., 2018). The use of 200 levels is significantly more computationally expensive, but, as shown in the results section, provides important improvements in the representation of passive tracers.

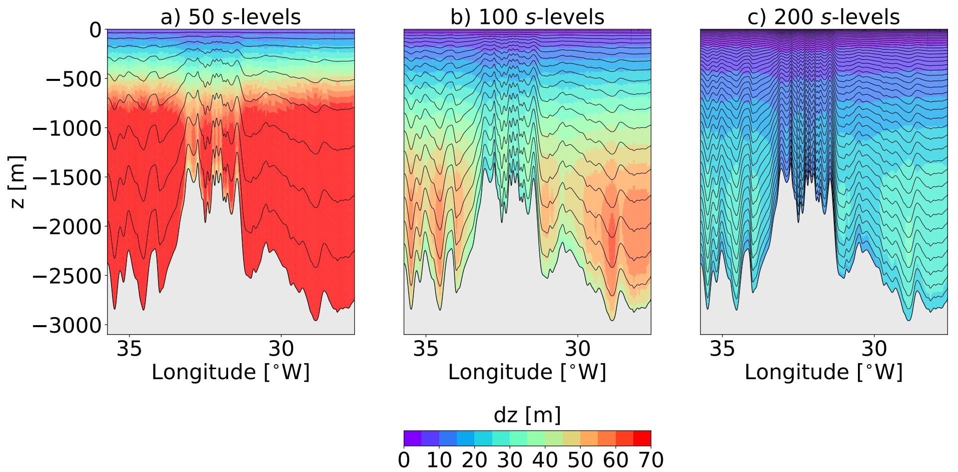

Figure 2. Vertical grid spacing using (a) 50 (b) 100 and (c) 200 s-levels. The vertical section is taken along the black dashed line in figure 1.

We use four combinations of tracer advective schemes (listed in Table 1):

- The up3 combination uses UP3 in the horizontal and SPLINES in the vertical for active and passive tracers.
- The rsup3 combination uses RSUP3 in the horizontal and SPLINES in the vertical for active and passive tracers.
- The rsup5 combination uses RSUP5 in the horizontal and SPLINES in the vertical for active and passive tracers.

- The weno5 combination uses RSUP5 and SPLINES for active tracers, and WENO5 in the horizontal and vertical for passive tracers.

Each simulation is labelled 'exp$i$-j' where $i \in \{50, 100, 200\}$ is the number of vertical levels and $j \in \{\text{up3}, \text{rsup3}, \text{rsup5}, \text{weno5}\}$ is the advective scheme combination. Each combination is run with 50, 100, and 200 vertical levels except for the first combination, which is run only with 100 levels (simulation exp100-up3). The rationale for doing so is that we anticipated that the RSUP3 scheme would give better results (less spurious diffusivity) than UP3. Although rotated schemes are rather specific to CROCO/ROMS, we wished to illustrate the effects of upstream and non-rotated schemes.

An additional simulation, exp200-rsup5-smooth, is run with a smoother bathymetry than in the baseline simulation. In exp200-rsup5-smooth, the raw bathymetry is smoothed with a Gaussian smoothing kernel with a radius of 15 grid points, equivalent to three times the characteristic scale. This choice is motivated by the result showing increased numerical mixing over steep topography. Figures 3a,b,c show the baseline bathymetry, the smoothed bathymetry, and the difference between the two. The difference in the distribution of topographic slopes is shown in Figure 3d. In the baseline topography, a significant number of grid points exhibit slopes greater than 10%, with some reaching up to 20%. In contrast, the modified topography limits slopes to a maximum of 11%, with only a few exceeding 10%. Despite this smoothing, the large-scale topographic features of the ridge are visually preserved. The steepness parameter using the smoother bathymetry is reduced from 0.062 to 0.02. The maximum value of the hydrostatic consistency condition rx_1 – sometimes called Haney number (Haney, 1991) – over the domain is ≈ 17 for exp200-rsup5 and ≈ 6 for exp200-rsup5-smooth.

2.3 Online diagnostic of diapycnal diffusivity

We define the effective diapycnal mixing as the sum of all sources of diapycnal mixing, including the parameterised and numerical mixing, following Capó et al. (2024). The effective diapycnal diffusivity, called K_{eff} in this article, is diagnosed online at each point in space and time during the model computation.

In a nutshell, we first diagnose the total potential temperature and salinity fluxes in three dimensions through each cell interface. We then estimate the purely advective part by calculating the contribution of the centered advection scheme at the nearest higher even order, whichever advective scheme is actually used in the simulation. The non-advective part is then defined as the total fluxes minus the estimated purely advective part. We then use these fluxes to reconstruct the buoyancy fluxes. Finally, we project the buoyancy fluxes in the direction orthogonal to the local isopycnal surfaces (based on local adiabatic density gradients) and divide by the norm of the buoyancy gradient to obtain an effective diapycnal diffusivity. These steps are described in the following sections.

2.3.1 Tracer fluxes

The first step is to calculate all fluxes for potential temperature T and salinity S. In the following we write the equations for the potential temperature T, but the equations for S are identical.

The calculation of fluxes is done by exactly closing the following budget for the volume-integrated tracer evolution in each model cell:

$$\begin{aligned}\frac{\Delta V^{n+1}T^{n+1} - \Delta V^n T^n}{\Delta t} = & - \vec{\nabla} \cdot \vec{F}^{Hadv} - \vec{\nabla} \cdot \vec{F}^{Vadv} \\ & - \vec{\nabla} \cdot \vec{F}^{Hmix} - \vec{\nabla} \cdot \vec{F}^{Vmix} - \vec{\nabla} \cdot \vec{F}^{Forc},\end{aligned} \tag{5}$$

Table 1. List of experiments

Configuration name	Number of s-levels	Horizontal advective scheme for momentum	Vertical advective scheme for momentum	Horizontal advective scheme for active tracers	Vertical advective scheme for active tracers	Horizontal advective scheme for passive tracers	Vertical advective scheme for passive tracers
exp100-up3	100	up3	splines	up3	splines	up3	splines
exp50-rsup3	50	up3	splines	rsup3	splines	rsup3	splines
exp100-rsup3	100	up3	splines	rsup3	splines	rsup3	splines
exp200-rsup3	200	up3	splines	rsup3	splines	rsup3	splines
exp50-rsup5	50	up3	splines	rsup5	splines	rsup5	splines
exp100-rsup5	100	up3	splines	rsup5	splines	rsup5	splines
exp200-rsup5	200	up3	splines	rsup5	splines	rsup5	splines
exp200-rsup5-smooth	200	up3	splines	rsup5	splines	rsup5	splines
exp50-weno5	50	up3	splines	rsup5	splines	weno5	weno5
exp100-weno5	100	up3	splines	rsup5	splines	weno5	weno5
exp200-weno5	200	up3	splines	rsup5	splines	weno5	weno5

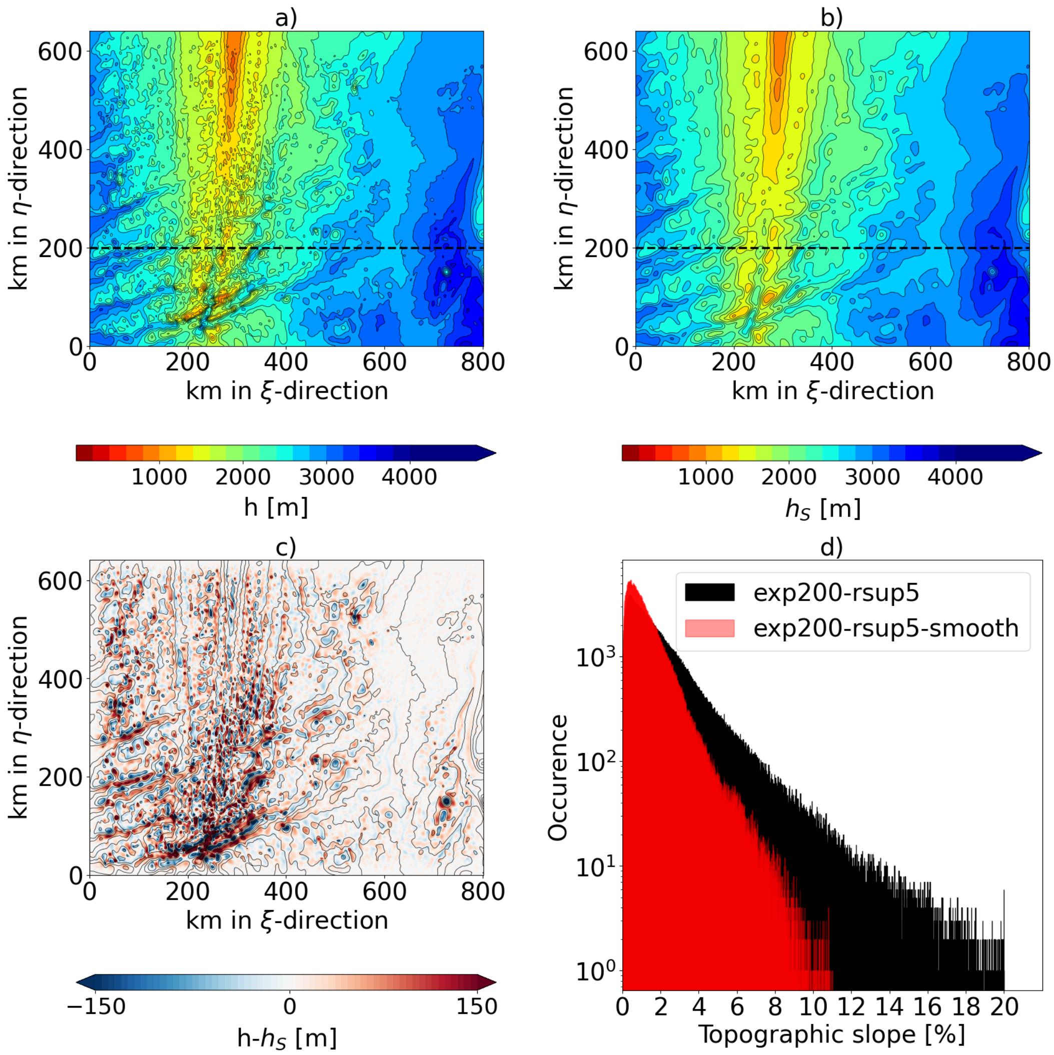

Figure 3. (a) Reference bathymetry, (b) smoothed bathymetry used in exp-200-rsup5-smooth, and (c) difference between reference and smoothed bathymetries. The black lines show the bathymetries at 200-meter intervals. (d) Histograms of the slope gradient for the unsmoothed bathymetry (black) and the smoothed bathymetry (red).

where $\Delta V^n = A\, H^n$ is the cell volume at time step n, H^n is the cell thickness and A is the horizontal cell area. The model uses a third-order predictor-corrector scheme, so that all terms on the right-hand side are calculated as functions of velocities and tracer values after the predictor step $(\vec{u}^{n+1/2}, T^{n+1/2}, S^{n+1/2})$.

The terms on the right-hand side are the divergence of the fluxes and include contributions from horizontal (Hadv) and vertical (Vadv) advective schemes, explicit horizontal mixing (Hmix), vertical mixing (Vmix), which primarily includes the parameterised mixing from KPP, but can also include other mixing due to the implicit vertical advection (Shchepetkin, 2015) and the stabilisation of the isoneutral diffusive operator (Lemarié et al., 2012a), and finally surface and bottom forcings (Forc). Most terms are available as fluxes at cell interfaces by default, except for vertical mixing, which is treated using an implicit algorithm. For simplicity, we integrate the resulting divergence term vertically to recover the flux through interfaces. The horizontal mixing term can be rotated along either geopotential (Marchesiello et al., 2009) or isopycnal (Lemarié et al., 2012b) surfaces when RSUP3/5 schemes are used. In such cases, an additional mixing term is added in the vertical (F_z^{Hmix}) in order to align the diffusive fluxes along the geopotential or isopycnal surfaces.

In the end, the total tracer flux is written in the model coordinates as:

$$\begin{aligned} \vec{F}^{tot} &= (F_\xi^{tot}, F_\eta^{tot}, F_z^{tot}) \\ &= (F_\xi^{Hadv} + F_\xi^{Hmix}, F_\eta^{Hadv} + F_\eta^{Hmix}, F_z^{Vadv} + F_z^{Hmix} + F_z^{Vmix} + F_z^{Forc}) \end{aligned} \quad (6)$$

with all terms defined at the corresponding cell interfaces (ξ, η, z).

2.3.2 Separating advective and non-advective fluxes

To separate the fluxes into an advective and a non-advective part, we make the assumption that the purely advective part can be approximated by a centered advective scheme in the horizontal (C4 if UP3/RSUP3 is used, or C6 if UP5/RSUP5/WENO5 is used) and a fourth-order centered parabolic spline reconstruction (SPLINES) in the vertical, such that:

$$\frac{\Delta V^{n+1} T^{n+1} - \Delta V^n T^n}{\Delta t} + \vec{\nabla} \cdot \vec{F^{adv}} = -\vec{\nabla} \cdot \vec{F}, \quad (7)$$

with a separation between advective ($\vec{F^{adv}}$) and non-advective fluxes ($\vec{F}$) defined as:

$$\begin{aligned} \vec{F^{adv}} &= (F_\xi^{C4/C6}, F_\eta^{C4/C6}, F_z^{SPLINES}) \\ \vec{F} &= (F_\xi^{Hadv} - F_\xi^{C4/C6} + F_\xi^{Hmix}, \\ &\quad F_\eta^{Hadv} - F_\eta^{C4/C6} + F_\eta^{Hmix}, \\ &\quad F_z^{Vadv} - F_z^{SPLINES} + F_z^{Hmix} + F_z^{Vmix} + F_z^{Forc}) \end{aligned} \quad (8)$$

Thus, $\vec{F}$ includes all non-advective terms from Equation 5, plus the implicit contribution from the advective fluxes, estimated as the difference between the advective scheme used and a centered advection scheme at the nearest higher even order. Note that in the case of the RSUP3 (resp. RSUP5) parameterisations, the CROCO code effectively calculates a C4 (resp. C6) advection for the tracers, then explicitly prescribes a rotated biharmonic diffusion scheme with flow-dependent hyperdiffusivity $B = \frac{1}{12} |U| \Delta^3$ (resp. $B = \frac{1}{20} |U| \Delta^3$) (Marchesiello et al., 2009). Thus, it is effectively a combination of a centered advective scheme with an explicit mixing operator.

2.3.3 Buoyancy fluxes

Non-advective buoyancy fluxes ($\vec{F^b}$) are then computed by combining potential temperature ($\vec{F^T}$) and salinity fluxes ($\vec{F^S}$) :

$$\vec{F^b} = -g(-\alpha \vec{F^T} + \beta \vec{F^S}), \quad (9)$$

where the thermal expansion coefficient $\alpha = -\frac{1}{\rho_0} \left(\frac{\partial \rho}{\partial T}\right)_S$ and the saline contraction coefficient $\beta = \frac{1}{\rho_0} \left(\frac{\partial \rho}{\partial S}\right)_T$ are computed using a local 3d linearization of the equation of state of the model (Shchepetkin & McWilliams, 2011).

2.3.4 Effective diffusivity

Finally, to get an effective diapycnal diffusivity, we project the buoyancy fluxes ($\vec{F^b}$) in the direction orthogonal to the isopycnal surfaces $\vec{n} = \frac{\vec{\nabla} b}{|\vec{\nabla} b|}$ and divide by the norm of the same gradient:

$$\begin{aligned} K_{eff} &= \vec{F^b} \cdot \frac{\vec{\nabla} b}{|\vec{\nabla} b|^2} \\ &= \frac{F^b_\xi \left.\frac{\partial b}{\partial \xi}\right|^{ad} + F^b_\eta \left.\frac{\partial b}{\partial \eta}\right|^{ad} + F^b_z \left.\frac{\partial b}{\partial z}\right|^{ad}}{|\vec{\nabla} b|^2}, \end{aligned} \tag{10}$$

where $\left.\frac{\partial b}{\partial .}\right|^{ad}$ are adiabatic buoyancy gradients (Equation 4.8 in Shchepetkin & McWilliams, 2011). The model's equation of state, which is based on a Taylor expansion of the equation of state described in Jackett and McDougall (1995), enables the direct separation of adiabatic and compressible effects in the spatial derivatives of density. Finally, the adiabatic buoyancy gradient norm is expressed in terms of horizontal gradients calculated at a constant depth, using the corresponding chain rules, which is equivalent to expressing the gradient norm in terms of orthogonal coordinates:

$$|\nabla b|^2_{i,j,k} = \left(\left.\frac{\partial b}{\partial \xi}\right|^{ad} - \frac{\partial z}{\partial \xi} \left.\frac{\partial b}{\partial z}\right|^{ad} \right)^2 + \left(\left.\frac{\partial b}{\partial \eta}\right|^{ad} - \frac{\partial z}{\partial \eta} \left.\frac{\partial b}{\partial z}\right|^{ad} \right)^2 + \left(\left.\frac{\partial b}{\partial z}\right|^{ad} \right)^2 . \tag{11}$$

Fluxes, gradients and their scalar products are naturally computed at the cell faces and averaged at the cell centre to obtain the effective diapycnal diffusivity.

In the (ideal) case where mixing is dominated by the vertical mixing parameterization ($\vec{F^b} \approx (0, 0, K_{KPP} \frac{\partial b}{\partial z})$) in the model coordinates, and if we assume that the horizontal buoyancy gradients (computed at constant depth) are small compared to the vertical stratification ($\left|\frac{\partial b}{\partial x}\right|, \left|\frac{\partial b}{\partial y}\right| \ll \left|\frac{\partial b}{\partial z}\right|$), we should recover $K_{eff} = K_{KPP}$. These assumptions may fail in the presence of strong lateral fronts and/or weak vertical stratification, which are common in the surface and bottom boundary layers (Baker et al., 2023), but we expect them to hold in the interior of the ocean.

Note that the method has several limitations. The first is that it is only valid as long as essentially dissipative advective schemes are used or that enough explicit mixing is included, since the mixing eventually introduced by dispersive errors of the centered advective schemes used to estimate the advective parts would not be taken into account by our method (Griffies et al., 2000). An example using directly a centered advective scheme (dominated by dispersive errors) without explicit diffusivity is included in Appendix B to illustrate this point. A second limitation is that our estimated advective part may also be affected by some dissipation implicit in the time stepping scheme, which would not be directly included in our effective diffusivity estimate. Finally, the diffusivity K_{eff} will be ill-defined in regions where the stratification vanishes and the norm of the adiabatic buoyancy gradient goes to zero. So diffusivity itself should be used with caution in the surface and bottom boundary layers, and it would be preferable to work directly with buoyancy fluxes in such cases.

However, a strong advantage is that we do not need a passive tracer patch to estimate K_{eff}, which allows us to analyse effective mixing in parts of the domain that do not depend on the tracer patch spreading. In section 3.2, we use the estimation of the online effective mixing K_{eff} to study the impact of the topography on the effective mixing over areas not covered by tracer patches.

2.4 Diagnostic of diapycnal diffusivity based on tracer release experiments

Independently of the online diagnosis of effective mixing, we use TREs to diagnose the effective diffusivity in the model (Getzlaff et al., 2010, 2012). In addition to providing a quantitative estimate of mixing, numerical TREs visually illustrate the diffusive and dispersive effects of the schemes.

Two passive tracers are released in each simulation. Tracer 1 is released over the abyssal plain in the Iceland Basin and tracer 2 is released over the Reykjanes Ridge. We expect the contrasting dynamics in these regions (smooth topography vs. rough topography) to produce different levels of mixing. The initial distributions of the tracer patches are Gaussian in density space:

$$c_{(t=0)} = \exp\left(-\frac{r^2}{2\sigma_r^2}\right)\exp\left(-\frac{(\rho-\rho_{target})^2}{2\sigma_\rho^2}\right) \tag{12}$$

where $r = \sqrt{(x-x_C)^2 + (y-y_C)^2)}$ and (x_C,y_C) is the location of the center of the patch, ρ_{target} is the initial target density, $\sigma_r = 2$ km, $\sigma_\rho = 0.01$ kg m^{-3}. The initial location of the tracers was chosen to keep the tracer patches in the domain as long as possible. Figure 4 shows the release of tracer 1 (Figure 4 a,e) and tracer 2 (Figure 4 c,g) and how the tracer patches are distributed vertically and horizontally 15 days after the release (4 b,f and d,h).

Two different methods are used to diagnose the diapycnal diffusivity experienced by each tracer. They are presented in the following.

2.4.1 Taylor estimate of diffusivity

Taylor (1922) studied the evolution of a tracer with a concentration c that follows the equation $\frac{\partial c}{\partial t} = \kappa\nabla^2 c$, where κ is the turbulent diffusivity. The main result is that κ is related to the rate of increase of the variance of the tracer distribution in the considered direction. To estimate the diapycnal diffusivity, oceanographers have considered the evolution of the tracer concentration in the diapycnal direction (e.g., Holmes et al., 2019). Following Ruan and Ferrari (2021), the estimated diffusivity K_{tr} can thus be written as:

$$K_{tr} = \frac{1}{2}\frac{1}{\langle|\nabla b|^2\rangle}\frac{\partial}{\partial t}\langle(b-\langle b\rangle)^2\rangle, \tag{13}$$

where b is buoyancy and $\langle\cdot\rangle$ is the tracer-weighted averaging operator:

$$\langle\cdot\rangle = \frac{\int\int\int \cdot\; c\,dx\,dy\,dz}{\int\int\int\; c\,dx\,dy\,dz}, \tag{14}$$

and the integral is taken over the full model volume.

For a constant mixing rate, we should recover $K_{tr} = \kappa$. Recently, Ruan and Ferrari (2021) revisited Taylor's theory in the general case where the mixing rate varies in space. In this case, the interpretation of K_{tr} is more complex. In the present simulations, KPP produces diapycnal mixing coefficients that rarely deviate from the background value in the ocean interior, where tracers 1 and 2 evolve. We therefore expect K_{tr} to be as close as possible to κ when no numerical mixing has been produced.

2.4.2 A one-dimensional model of tracer spreading across isopycnals

We also use an alternative method to estimate the diapycnal diffusivity K_{fit} based on a one-dimensional model describing the tracer concentration evolution c in buoyancy space. This model has been widely used in field TREs (e.g., Ledwell & Watson, 1991) and in virtual TREs (Holmes et al., 2019). It reads:

$$\frac{\partial \overline{c}}{\partial t} + \left(\overline{w} - \overline{\frac{\partial K_{fit}}{\partial h}} \right) \frac{\partial \overline{c}}{\partial h} = \overline{K_{fit}} \frac{\partial^2 \overline{c}}{\partial h^2}, \tag{15}$$

where w is the vertical velocity and the overbar denotes an average over buoyancy classes at a given height h above the buoyancy class targeted at the tracer release. A mean stratification profile $\bar{N}^2$ is used to convert between h and b such that $h = b/\bar{N}^2$. The diapycnal diffusivity $\overline{K_{fit}}$ is assumed to be a linear function of h, $\overline{K_{fit}} = \overline{K_0} + h\overline{\frac{\partial K_{fit}}{\partial h}}$, where K_0 is the diapycnal diffusivity at the target buoyancy. We use the method and algorithm described in Appendix B in Holmes et al. (2019) to infer K_{fit}. Briefly, the first stage consists in summing the tracer concentration in h coordinates. The second stage consists in using a least-square method on discretized Equation 15 at each time step to find the three parameters $\overline{K_0}$, $\overline{w}$ and $\overline{\frac{\partial K_{fit}}{\partial h}}$ that minimize the distance between the 'observed' $\overline{c}$ inferred from the simulation and the 1-d model prediction from the initial distribution.

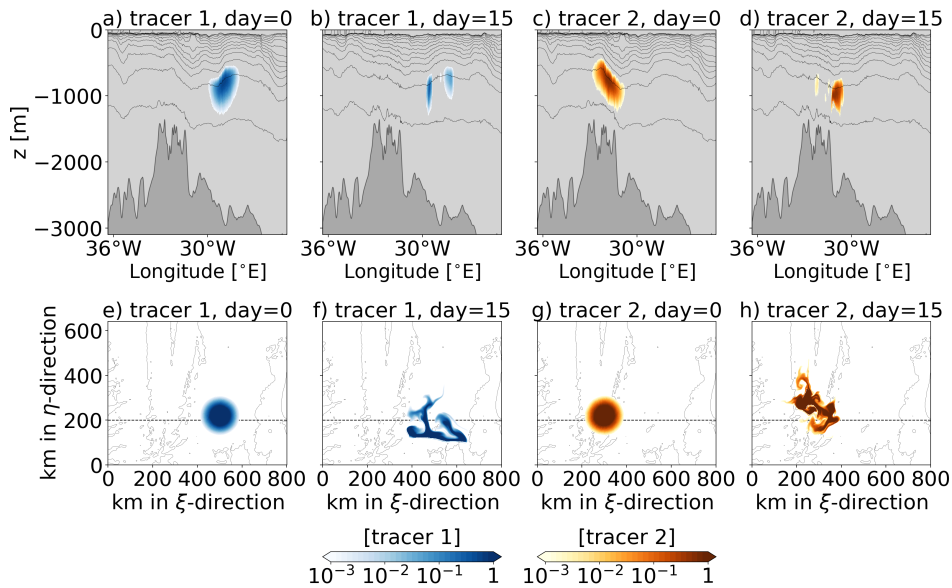

Figure 4. Vertical (a-d) and horizontal (e-h) snapshots of tracer concentration from the configuration exp200-rsup5 for a,e) tracer 1 at release, b,f) tracer 1 after 15 days, c,g) tracer 2 at release, and d,h) tracer 2 after 15 days. The solid black lines in the upper panels represent the potential density field referenced at the surface from 1026.5 kg m^{-3} to 1028.4 kg m^{-3} with variations of 0.1 kg m^{-3}. The vertical section used is the black dashed line in panels (e-h). Tracer patches are vertically integrated in the lower panels and the solid black lines represent the contour of the bathymetry every 1000 meters.

3 Results

3.1 Overview of the simulated dynamics

We first present an overview of the dynamics in the region. The large-scale and mesoscale dynamics are qualitatively similar in all simulations, and we show examples from only one simulation (exp200-rsup5).

Mesoscale currents are remarkably barotropic, with horizontal currents extending from below the surface mixed layer to the seafloor (Figures 5a and 5b), as is characteristic of high-latitude gyres (Le Corre et al., 2020). The vertical velocity (w) patterns have smaller horizontal and vertical scales with large amplitudes throughout the whole water column (Figure 5c). It is largely the signature of energetic internal waves, either generated by flow-topography interactions above the Reykjanes Ridge as internal tides or lee waves or by the strong wind events in the gyre (Vic et al., 2021). The stratification, represented by N^2, is enhanced in the thermocline and decreases smoothly with depth (Figure 5d). It is minimal in the surface and bottom mixed layers, with values eventually reaching zero and locally becoming negative. The vertical shear of horizontal velocity, S^2, is enhanced in the thermocline and in the boundary layers (Figure 5e). Distinct thin layers (≈100 m, a few vertical grid points) of elevated shear are characteristic of internal waves, especially near-inertial waves (Alford et al., 2016).

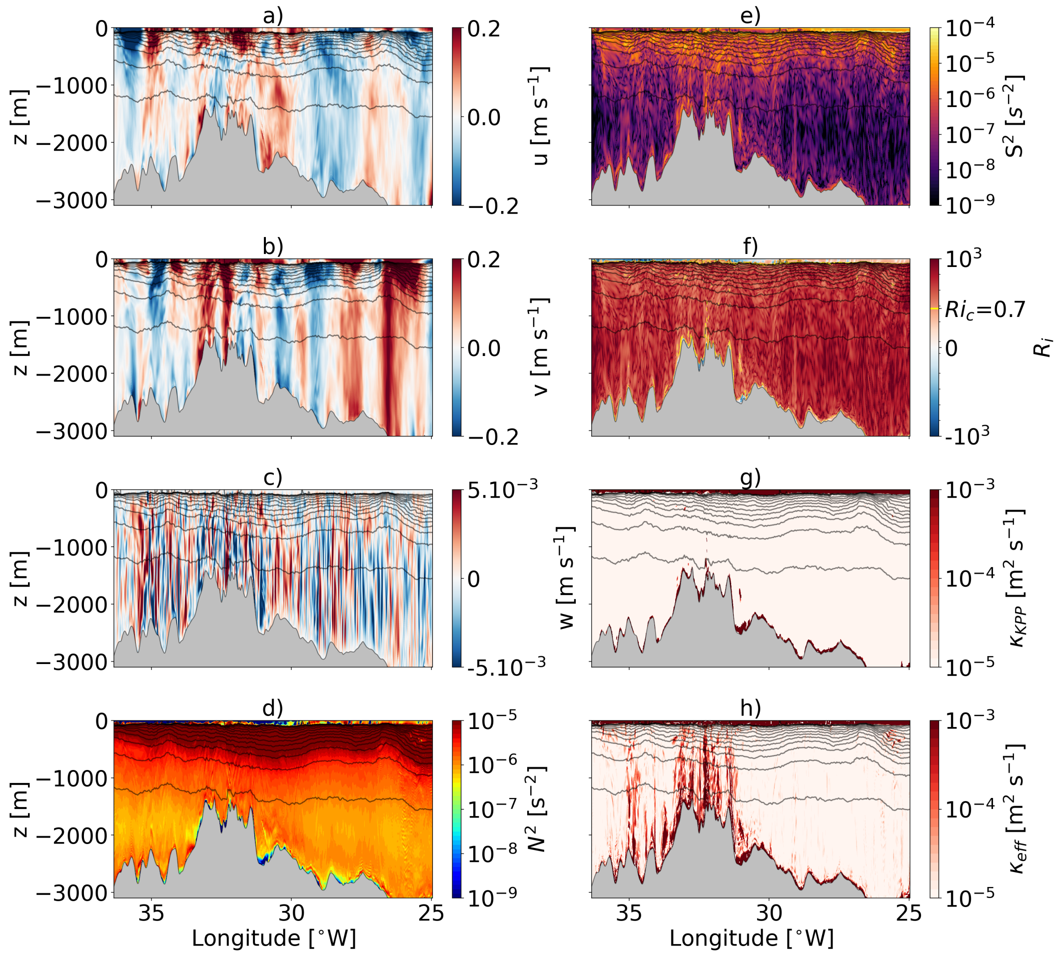

Figure 5. Vertical section of (a) zonal velocity u (in m/s), (b) meridional velocity v (in m/s), (c) vertical velocity w (in m/s), (d) Brunt-Vaisala frequency N^2 (in s^{-2}), (e) vertical shear of horizontal velocity S^2 (in s^{-2}), (f) Richardson number Ri, (g) the parameterised mixing K_{KPP}, and (h) the effective mixing K_{eff} for the exp200-rsup5 experiment 10 days after tracer release. The solid black lines in the upper panels represent the potential density field referenced at the surface from 1026.5 kg m^{-3} to 1028.4 kg m^{-3} with variations of 0.1 kg m^{-3}. The vertical section is taken at the black dashed line in figure 1.

The Richardson number $Ri = N^2/S^2$ compares the destabilizing strength of shear with the stabilizing effect of stratification. Regions of strong shear and weak stratification are prone to shear instability and mixing, these regions correspond to values of Ri less than the critical value Ri_c (Figure 5f). In the boundary layers we often have $Ri < Ri_c$, while in the interior $Ri > Ri_c$ almost everywhere, except in some thin shear layers described above. Thus, in the interior, the resulting diffusivity coefficient computed by KPP, K_{KPP}, is predominantly equal to its background value of $K^w = 10^{-5}$ m^2 s^{-1} (section 2.1), except for a few localized spots (Figure 5g). In the boundary layers, K_{KPP} reaches high values up to 10^{-1} m^2 s^{-1} where convective instabilities occur. The effective mixing K_{eff} exceeds the parameterized mixing K_{KPP} by several orders of magnitude over the entire water column when the seafloor topography is rough (Figure 5h vs 5g). This is discussed in details in Section 3.2.

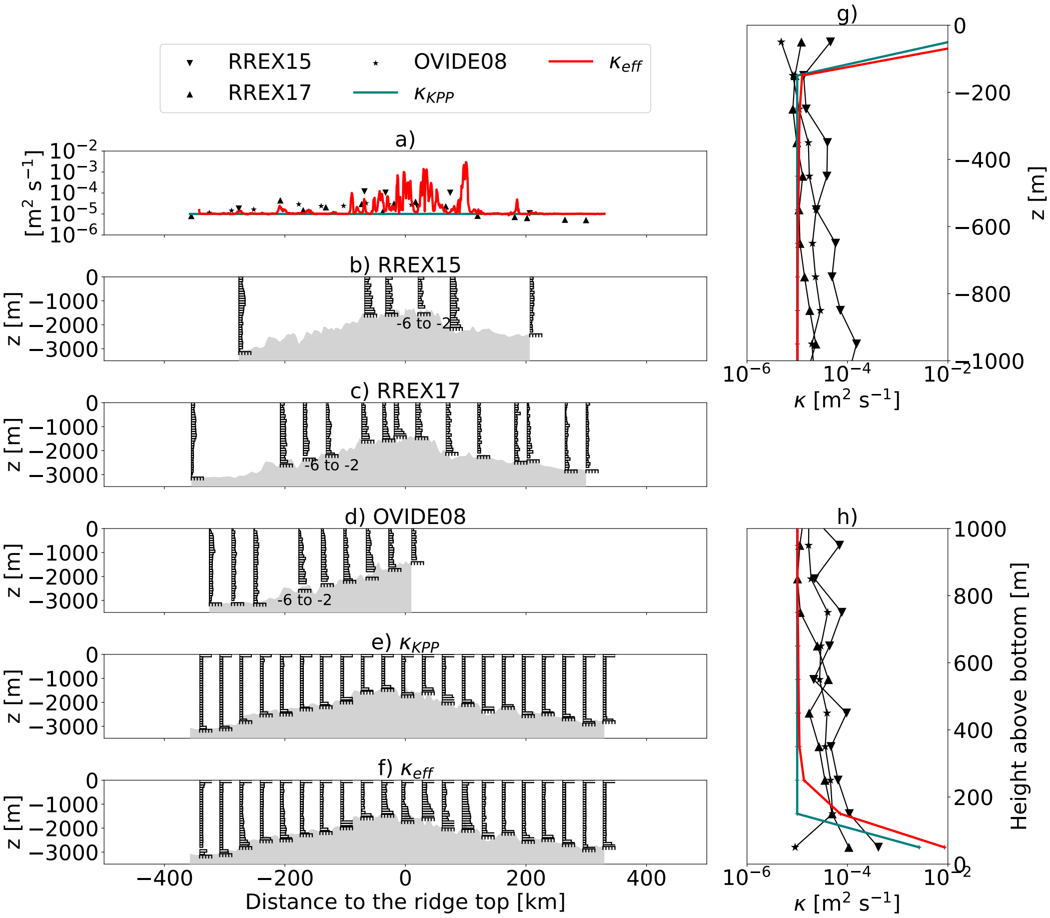

Figure 6. Comparison of observed diffusivities from campaigns RREX15, RREX17, and OVIDE08, with parameterized diffusivities from KPP and effective diffusivity K_{eff} in the exp200-rsup5 configuration along the blue section visible in figure 1. Median diffusivities as a function of (a) the distance to the ridge, (g) the depth and (h) the height above bottom for the RREX15, RREX17 and OVIDE08 campaigns, the KPP diffusivity, and the effective diffusivity K_{eff}. The median is computed over 29 days for K_{KPP} and K_{eff}. Vertical profiles of diffusivities estimated from (b) RREX15 (c) RREX17, and (d) OVIDE08 observations. Median values from 29 days of exp200-rsup5 for (e) the KPP diffusivity and (f) the effective diffusivity K_{eff}. The vertical profiles are shown every 20 km in panels e and f.

To assess the realism of the parameterized mixing coefficients K_{KPP}, we compared them with microstructure estimates from three cruises: OVIDE08 (Ferron et al., 2014), RREX15 (Branellec & Thierry, 2016), and RREX17 (Branellec & Thierry, 2018). It should be noted, however, that matching diffusivities do not necessarily guarantee better realism of the model's large-scale circulation, as the model has to compensate for biases and numerical errors. Nevertheless, it is instructive to compare the result of a parameterisation such as KPP when used in a high-resolution regional model with actual measurements. Microstructure-based estimates are computed following Osborn (1980):

$$\kappa = \Gamma \frac{\epsilon}{N^2} \tag{16}$$

where $\Gamma = 0.2$ is the mixing efficiency (Gregg et al., 2018), ϵ is the turbulent energy dissipation and N^2 is the stratification. Both ϵ and N^2 are estimated from probes mounted on a vertical microstructure profiler (instrument manufactured by Rockland Scientific International Inc.). Details of the processing can be found in Ferron et al. (2014). The three cruises sampled the same section across the Reykjanes Ridge (shown in Figure 1). All products are shown in Figure 6. Data are binned on the same vertical grid with 100 m bins to facilitate comparison. The in situ estimates all show contrasting profiles between the Reykjanes Ridge, the Iceland Basin and the Irminger Sea. Over the ridge, mixing increases from below the thermocline (10^{-5} m^2 s^{-1}) down to the bottom (10^{-4} m^2 s^{-1}), which is typical of internal tide-driven mixing over mid-ocean ridges (Waterhouse et al., 2014). Over the abyssal plain in the Iceland Basin, mixing is reduced and is close to 10^{-5} m^2 s^{-1} throughout the whole water column. Overall, K_{KPP} is close to κ in the ocean interior and off the ridge, but is smaller over the ridge in the $\approx$1000 m above the seafloor. The model likely misses some enhanced mixing events associated with internal wave breaking over rough topography and does not generate enough vertical shear to achieve sufficiently low Richardson numbers. While the energy levels associated with internal wave activity are expected to be well resolved at least for the near-inertial and semi-diurnal tidal peaks (see the comparison between model and moorings in Barkan et al. (2021b) with a very similar setup), the internal wave continuum is likely to be slightly underestimated due to the lack of vertical/horizontal resolution (Nelson et al., 2020). A solution to improve the realism of the internal wave field and the associated diffusivities might be to turn off the background diffusivity and increase the critical Richardson number, as suggested in Thakur et al. (2022) and Momeni et al. (2024).

The effective mixing, K_{eff}, closely matches the KPP mixing and observational data away from the ridge, indicating that numerical mixing is minimal (less than 10^{-5} m^2 s^{-1}), even in the presence of energetic, high-frequency isopycnal oscillations in the simulation. Over the ridge, however, the effective mixing exceeds the KPP mixing and aligns more closely with observations (approximately 10^{-4} m^2 s^{-1}) (Figure 6a), highlighting the presence of numerical mixing over topographic slopes in regions of enhanced in-situ diffusivities. While this leads to more realistic average diffusivities overall, it can locally result in higher values, up to $\approx 10^{-3}$ m^2 s^{-1}, which may exceed the observed in-situ diffusivities. This numerical mixing arises from various discretization errors and implicit advective diffusion, which can partially compensate for deficiencies in explicit parameterizations. Although some of this numerical mixing might be beneficial, it is problematic because it cannot be directly controlled. Therefore, it's crucial to evaluate it based on the model setup and configuration to ensure it remains within realistic bounds. In the next section, we provide a more detailed investigation of numerical mixing for the previously presented set of simulations.

3.2 Parameterized vs effective mixing

The differences between the effective diffusivity K_{eff} and the parameterized one K_{KPP} are strongest above the steepest slopes of the seafloor topography above the Reykjanes Ridge, over a depth extending from the seafloor to several hundred meters or more above (Figure 5). We quantify this discrepancy more systematically by computing some statistics of K_{eff} in two contrasting regions, above the ridge and above the abyssal plain of the Iceland Basin, for the simulations with 50, 100 and 200 levels (Figure 7). Overall, it confirms the impression that K_{eff} departs from K_{KPP} above the ridge in the lowermost 1000 m above the seafloor (10^{-4} m^2 s^{-1} vs 10^{-5} m^2 s^{-1}), but is close to K_{KPP} in the abyssal plain. Also, note that K_{eff} has a larger spread above the ridge than above the abyssal plain throughout the whole water column. We will see that this is related to the wider distribution of topographic slopes over the ridge as compared to the rather homogeneously flatter abyssal plain.

The number of s-levels affects the vertical diffusivity profiles. Over the abyssal plain, increasing the number of s-levels slightly reduces the effective mixing, especially when moving from 50 to 100 levels. A further increase to 200 levels shows a modest improvement, with the effective mixing becoming more similar to the parameterized mixing. However, notable discrepancies between effective and parameterized mixing remain above the ridge, regardless of the vertical resolution. In fact, increasing the number of levels from 100 to 200 does not significantly reduce these differences and, more surprisingly, actually amplifies them in the lower 800 meters.

The increase of K_{eff} with increasing vertical resolution above the ridge is counterintuitive. In fact, this is related to numerical constraints on the isoneutral rotation of the diffusive part of the RSUP3 and RSUP5 advection schemes (see section 2.1). Recall that the constraint is linked to parameters s_m and α_m and that the rotation is effective only if these parameters are smaller than critical values $s_c = 1$ and $\alpha_c = 0.05$. Figure 8 shows K_{eff} and the parameters s_m and α_m for simulations exp50-rsup5 and exp200-rsup5. There is a clear contrast between the abyssal plain, where $s_m < s_c$ and $\alpha_m < \alpha_c$, and the ridge, which has large areas with $s_m > s_c$ and $\alpha_m > \alpha_c$. Two reasons can be given to explain these differences. First, the ridge seafloor topography has larger gradients, hence larger s-layer slopes and larger grid aspect ratios and larger s_m throughout the water column. Second, the stronger currents and the enhanced internal wave activity over the ridge means that isopycnal slopes can be locally steeper than in the rest of the domain (Figure 5). Overall, the grid points that do not satisfy equations 1 or 2 are associated with enhanced K_{eff} (Figure 8). Also, while increasing the number of vertical levels does not directly change the isopycnal slope (Figure 8g vs Figure 8h), it does change the grid slope ratio, which includes Δ_z in the denominator(Figure 8d vs Figure 8e). This has the direct effect of further increasing K_{eff} (Figure 8a vs Figure 8b).

The effects of these constraints on the isopycnal slope and grid slope ratio are confirmed more quantitatively by examining the time-averaged ratio between effective and parameterized mixing as a function of isopycnal slope α_m and grid slope ratio s_m (Figure 9). The ratio is systematically greater than one for points where the isopycnal slope and grid slope ratio exceed their respective critical values. The grid slope ratio s_m is the most limiting constraint for most points, as suggested in Lemarié et al. (2012a).

Another interesting feature that emerges from increasing the number of levels is the sharpening of the contrast between interior and boundary mixing. The bottom boundary layer is better defined by the KPP scheme in the 100- and 200-level simulations than in the 50-level simulation (green lines in Figure 7). This is likely to have important implications for water mass transformation near the bottom (Baker et al., 2023).

3.3 Spreading of the passive tracers

We now examine the behavior of the two passive tracers released in the simulation, one over the abyssal plain and the other above the ridge.

The tracer concentration for the tracer released over the abyssal plain (tracer 1) is shown in Figure 10 10 days after release across all simulations. The most striking fea-

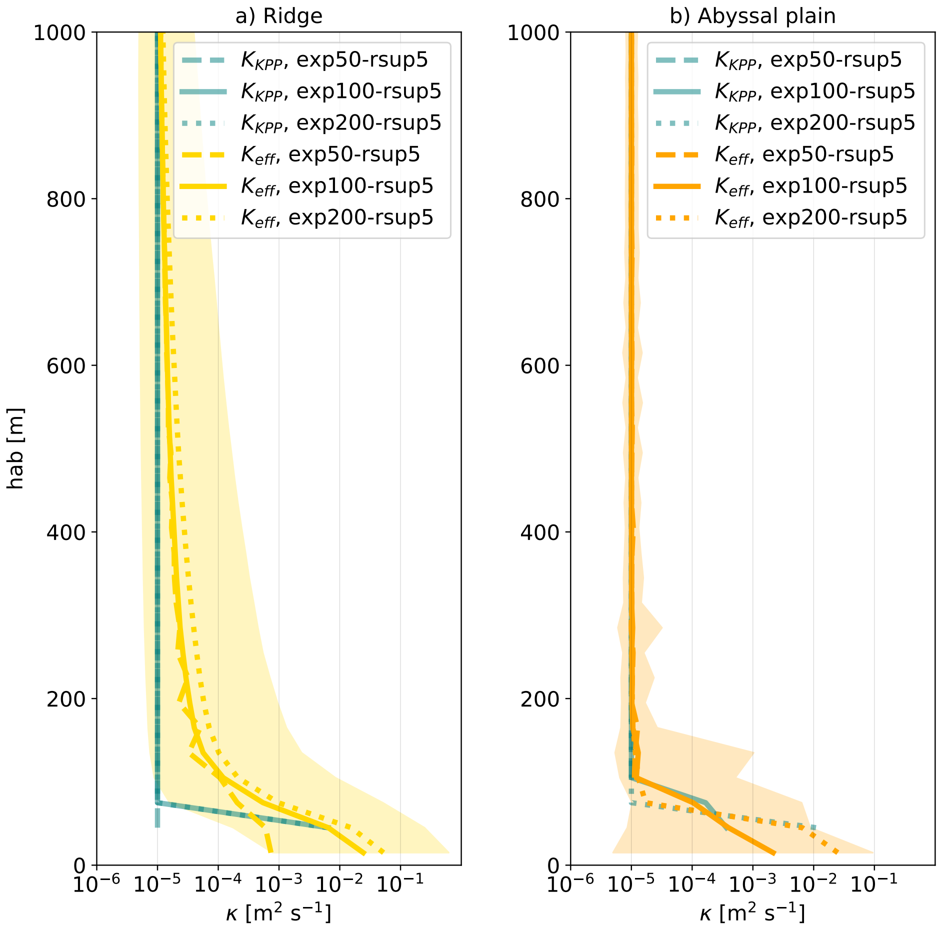

Figure 7. Median value of (green) the parameterized mixing K_{KPP} and (yellow, orange) the effective mixing K_{eff} as a function of height above bottom (hab) averaged over (a) the ridge (yellow dashed rectangle in Fig. 1), and (b) the abyssal plain (orange dashed rectangle in Figure 1) for configurations exp50-rsup5, exp100-rsup5 and exp200-rsup5. The (a) yellow (b) orange shadow areas are the 10^{th} and 90^{th} percentiles of the effective mixing using configuration exp100-rsup5, considering (a) the ridge and (b) the abyssal plain areas. Above 200 meters above the seafloor the 10^{th} and 90^{th} percentiles of the effective mixing are almost identical for all configurations, while exp50-rsup5 has wider percentiles values below 200 meters.

ture is the pronounced dispersive patterns observed at the lowest vertical resolution (50 levels) when using the upstream horizontal advection schemes (RSUP3 and RSUP5) in combination with the SPLINES vertical advection scheme for both active and passive tracers. This dispersion is likely a result of the combination between a fourth-order compact scheme in the vertical with low dissipation and the upstream horizontal advection schemes in the horizontal. Indeed, the hyperdiffusivity inherent to these schemes (Boyd, 1994; Jiménez, 1994) could lead to strong overshoots in the presence of large grid-scale tracer gradients. Doubling the number of vertical levels to 100 levels significantly reduces this effect, with further improvement at 200 levels. As expected, the non-rotated UP3 scheme actually leads to more spurious diapycnal mixing than the RSUP3 scheme (compare Figure 10d with Figure 10e). The weno5 scheme combination is generally more diffusive, especially noticeable at 50 levels. However, it effectively reduces oscillations and prevents negative concentrations (Figure 11) compared to the upstream schemes.

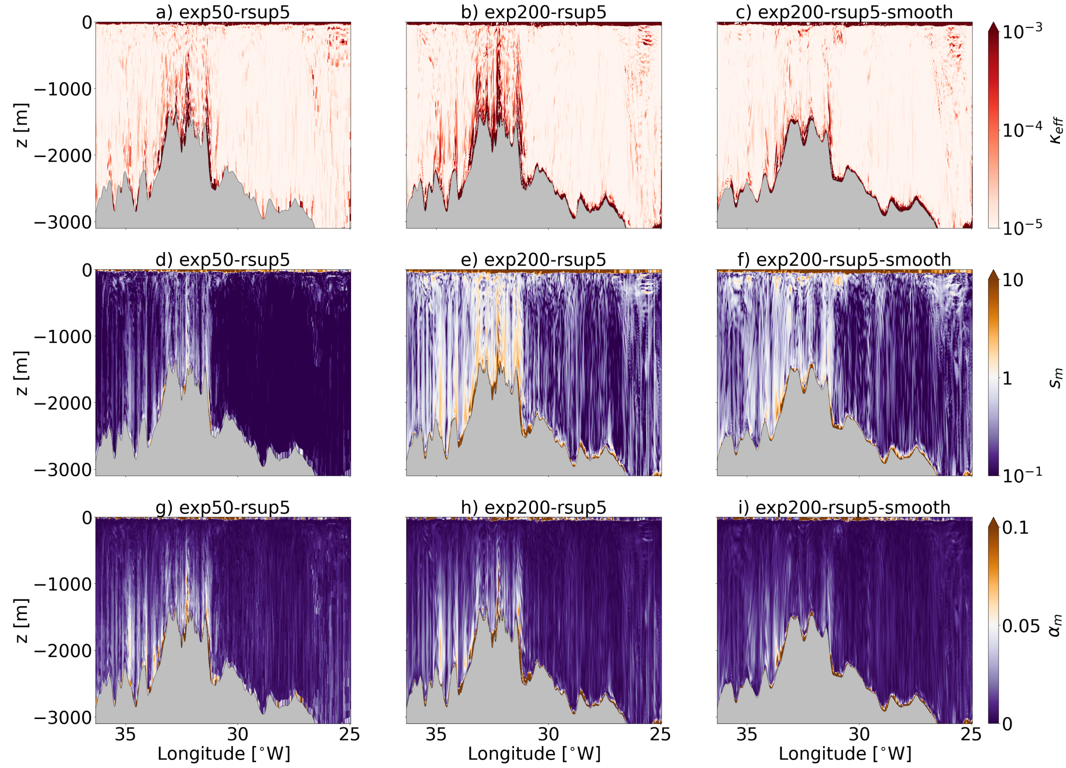

Figure 8. Snapshot at 10 days of vertical sections of (a-c) K_{eff}, (d-f) the grid slope ratio s_m, and (g-i) the isopycnal slope α_m, for (a,d,g) exp50-rsup5, (b,e,h) exp200-rsup5, and (c,f,i) exp200-rsup5-smooth. The values $\alpha_m = 0.05$ and $s_m = 1$ are the critical values. The vertical section is taken at the black dashed line in figure 1.

Increasing the number of levels to 100 or 200 levels significantly improves the tracer representation. Oscillations at the vertical grid scale in the tracer concentration between its core and the seafloor are attenuated, which we interpret as a reduction of numerical dispersion – this is especially true for the upstream schemes. Overall, the three combinations of advective schemes are visually similar when 200 vertical levels are reached. Nonetheless, we would recommend to use WENO5 for tracer advection if one strictly needs to avoid negative concentrations caused by dispersion.

The tracer concentration for the tracer released over the ridge (tracer 2) is shown in Figure 12. Overall, the two tracers show the same characteristics with respect to the advection schemes used. Importantly, the differences between the combinations of schemes are most pronounced when 50 levels are used, and gradually disappear when 100 and 200 levels are used. In all cases, the results seem to converge between 100 and 200 levels.

3.4 Numerical mixing above the abyssal plain

We now compare the parameterized diffusivity in the model (K_{KPP}) with our different estimates for the diapycnal diffusivity: the effective diffusivity K_{eff} based on the online buoyancy budget and the tracer-based diapycnal diffusivities K_{fit} and K_{tr} diagnosed from the tracer spreading across isopycnals (Section 2.4).

These different estimates are shown in Figure 13 for tracer 1, released over the abyssal plain. K_{KPP} and K_{eff} are averaged over the tracer patch using the tracer-weighted av-

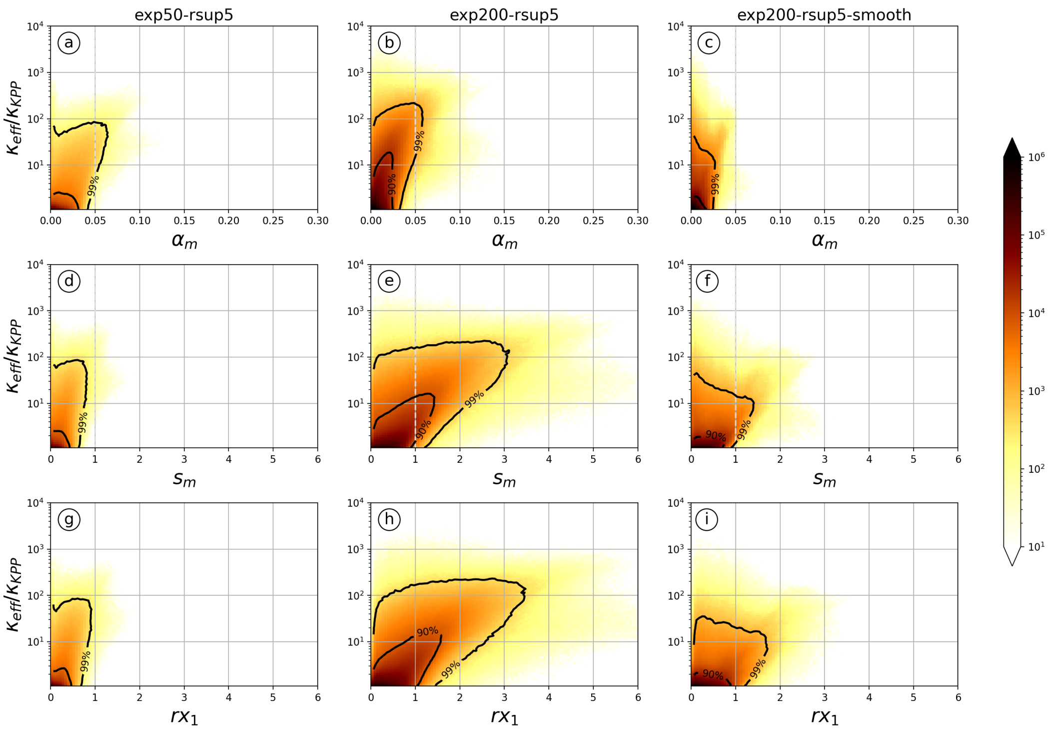

Figure 9. Binned histograms for the ratio of the time mean effective and parameterized diffusivities versus (a-c) the isopycnal slope α_m, (d-f) the grid slope ratio s_m, and (g-i) the hydrostatic consistency condition rx_1, for (a,d,g) exp50-rsup5, (b,e,h) exp200-rsup5, and (c,f,i) exp200-rsup5-smooth. Points less than 100 m above the bottom and less than 200 m below the surface have been excluded. The dashed grey lines show the critical values for the isopycnal slope and grid slope ratio. The black contours are the integrated domains containing 90% and 99% of the points.

eraging operator from Equation 14. As there are weighted by the tracer concentration, K_{KPP} and K_{eff} can thus be interpreted as the average diffusivity coefficients seen by the tracer. Thus, while K_{KPP} should represent the diffusivity experienced by the tracer in the absence of additional diffusivity due to the advection schemes, K_{eff} represents the actual, effective mixing, which is the sum of the prescribed mixing (from KPP) and the numerical mixing due to the advection schemes. The four estimates are diagnosed for each time step over the first 15 days after tracer release, and box plots represent their distribution over this period.

Confirming what we have seen so far, K_{KPP} and K_{eff} are close to 10^{-5} m^2 s^{-1} (background mixing in KPP) in all simulations, regardless of the number of vertical levels and the combination of schemes, except for exp100-up3. The latter simulation uses the non-rotated horizontal schemes and hence produces spurious mixing (Marchesiello et al., 2009). This spurious mixing is highlighted by the departure of K_{eff} from K_{KPP}. For all other simulations, the fact that K_{eff} approaches K_{KPP} is a good indication that numerical mixing remains small in the abyssal plain in all configurations.

The two tracer-based estimates show large differences with K_{KPP} and K_{eff} at the coarser vertical resolution (50 levels), with diffusivities up to two orders of magnitude larger (comparable to what is seen in Bracco et al. (2018), for example). However, increasing the number of vertical levels significantly reduces the mixing experienced by the

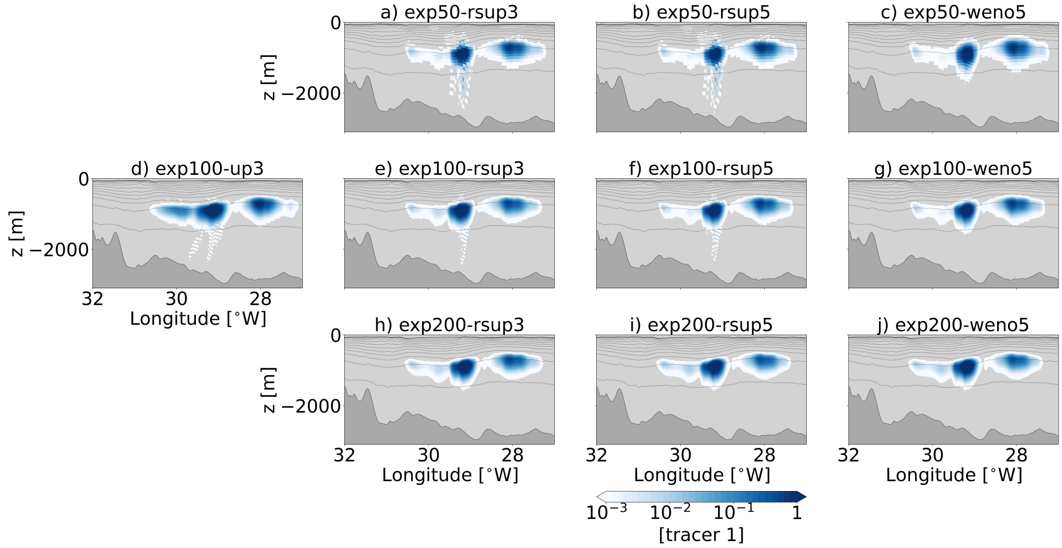

Figure 10. Vertical section of tracer 1 after 10 days for each configuration along the section shown in Figure 1. The tracer patch is summed over 10 grid points in the along ridge direction. Tracer concentration smaller than 10^{-4} are not shown.

tracer. Overall, doubling the number of vertical levels from 50 to 100 reduces the diffusivity experienced by tracer 1 by an order of magnitude, and again when doubling from 100 to 200. This is true for all the advection schemes used. With 50 levels, K_{tr} reaches median values of $1-3\times10^{-3}$ m^2 s^{-1}, which are two orders of magnitude larger than the expected diffusivity (K_{KPP}). With 200 levels, K_{tr} is reduced to $1{-}4{\times}10^{-5}$ m^2 s^{-1}, much closer to the parameterized values.

For the same vertical resolution, the weno5 combination is on average 2-3 times more diffusive than the rsup3 and rsup5 combinations. Even with 200 levels, the tracer-based estimates do not converge to the effective mixing diagnosed in the simulation. This is partly due to the fact that they do not benefit from the isoneutral rotation of the diffusive part as the RSUP3/5 schemes do, so even if the diffusive part is strongly reduced when the resolution is increased, it is still oriented along s-levels instead of isopycnals. The differences between rsup3 and rsup5 are small, although K_{tr} is slightly larger for rsup5. While the dissipative part of the advection scheme is expected to be about twice as small for rsup5 (visible in the slightly smaller effective diffusivities), the dispersive effects are stronger for the 5th order scheme, leading to slightly larger tracer-based diffusivities.

Note that K_{fit}, which is expected to be comparable to K_{tr}, is much smaller for the 50- and 100-level simulations using rsup3 and rsup5. We attribute this discrepancy to a limit of the 1-d fit method when using a coarse vertical grid resolution in the presence of dispersive errors. Indeed, the 1-d distribution of the tracer in buoyancy space does not smoothly fit a Gaussian distribution (see Appendix C), a requirement for the method to be reliable (Holmes et al., 2019). The difference between K_{tr} and K_{fit} is much smaller for exp50-weno5, which uses a more diffusive scheme. The difference between K_{tr} and K_{fit} disappears for exp200-rsup3 and exp200-rsup5. This confirms the visual impression in Figure 10 that the dispersive effect of the upstream/splines combination disappears with 200 levels.

Naively, we might have expected K_{tr} (and to lesser extent, K_{fit}) to be closer to K_{eff} for the rsup3 and rsup5 simulations even with 50 and 100 levels. Indeed, these sim-

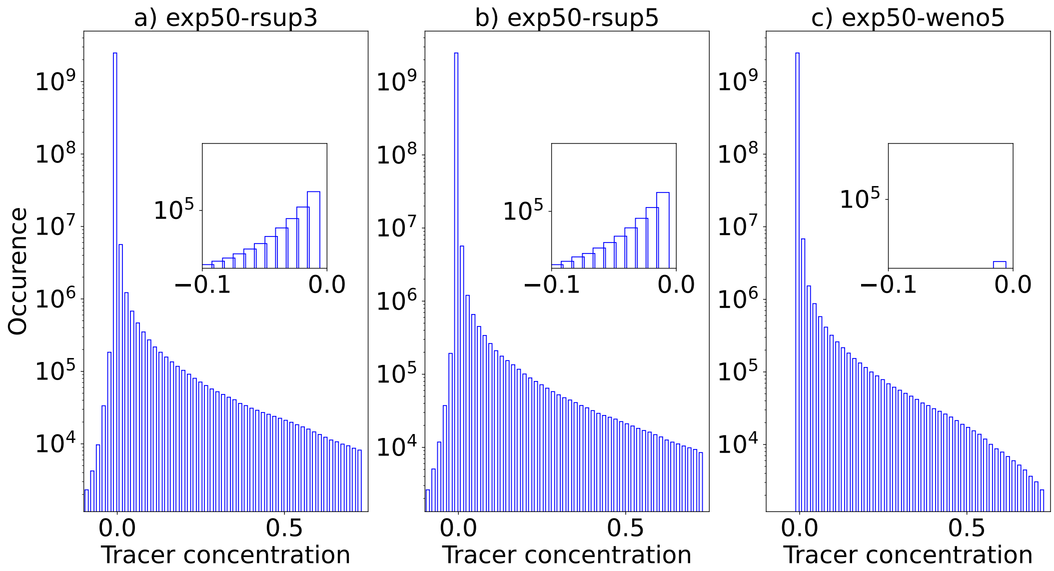

Figure 11. Histogram of tracer 1 concentration over 40 days for configurations: a) exp50-rsup3 b) exp50-rsup5, and c) exp50-weno5. The inset shows a zooming view of the negative concentrations.

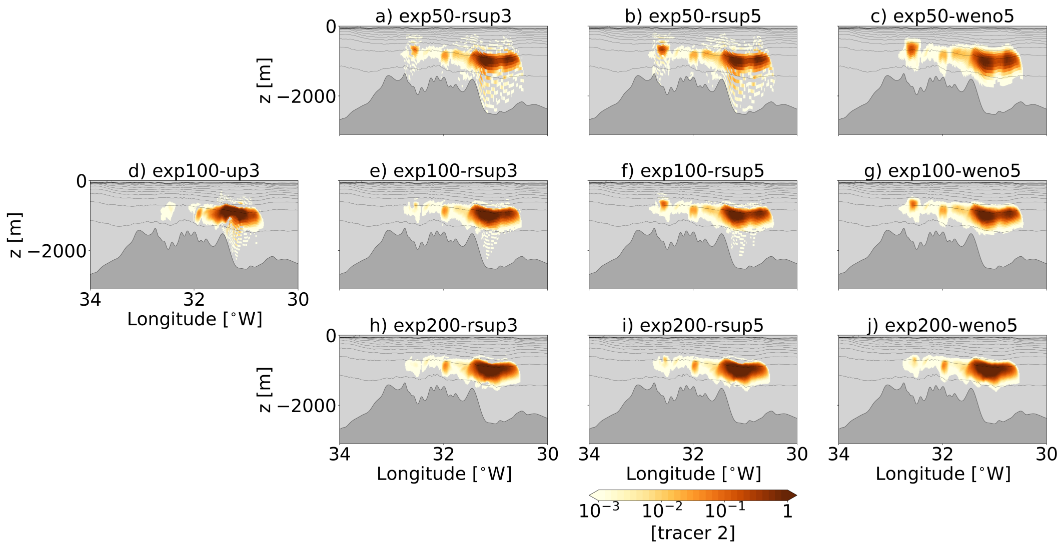

Figure 12. Same as Figure 10 but for tracer 2, released above the ridge.

ulations use the same advection schemes for the active tracers, used to diagnose K_{eff}, and for the passive tracers. However, the vertical scales of the passive tracer gradients are much smaller than the temperature and salinity gradients at comparable depths. This leads to increased dispersion of the passive tracers, which ultimately leads to increased tracer variance in buoyancy space, hence the larger values of K_{tr} as compared to K_{eff}. An underestimation of K_{eff} in the presence of dispersive effects could be another factor contributing to the discrepancy, although there are no obvious dispersive patterns observed for T and S in the interior above the abyssal plain. This remains to be investigated using other methods for diagnosing numerical mixing, such as the general analysis of discrete variance decay (Burchard & Rennau, 2008; Klingbeil et al., 2014; Baner-

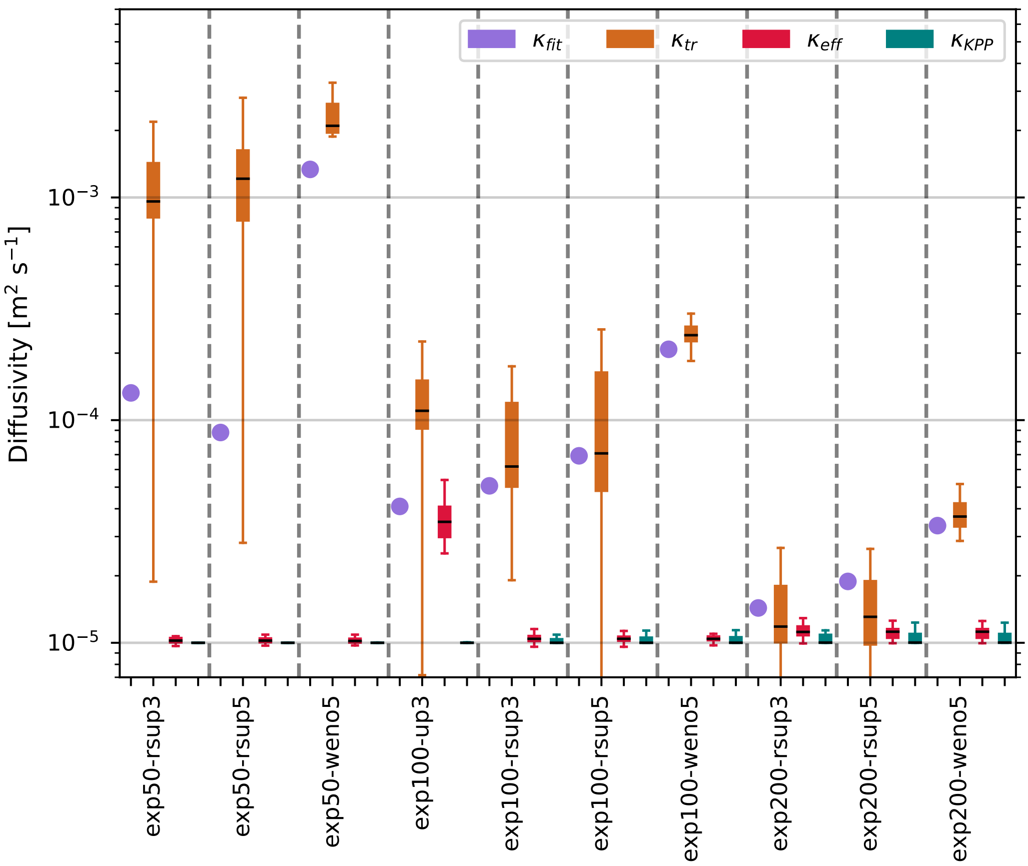

Figure 13. Estimation of the diffusivities experienced by tracer 1, released above the abyssal plain, for configurations exp50-rsup3, exp50-rsup5, exp50-weno5, exp100-up3, exp100-rsup3, exp100-rsup5, exp100-weno5, exp200-rsup3, exp200-rsup5, exp200-weno5. The parameterised diffusivity K_{KPP} is in green, the online diagnosed effective diffusivity K_{eff} is in red, and the two tracer-based diffusivities K_{tr} and K_{fit} are in orange and purple. K_{eff} and K_{KPP} are weighted by the tracer concentration following Equation 14. Diffusivities are considered for the first 15 days. For each box plot, the extremities of the box represent the minimum and the maximum values of the distribution and the box shows the first quartile, the median and the third quartile of the distribution.

jee et al., 2024), indirectly using a full water mass transformation budget as described in Drake et al. (2025), or via idealized experiments such as those described in Griffies et al. (2000).

3.5 Numerical mixing above the ridge

We expect higher levels of numerical mixing above the ridge, where tracer 2 is released, as seen in section 3.2. The tracer-weighted parameterised mixing K_{KPP} (Figure 14) is not much different than above the abyssal plain, and remains close to its background value (10^{-5} m^2 s^{-1}), showing that tracer 2 does not enter the bottom boundary layer. However, the effective mixing seen by tracer 2, K_{eff}, differs from K_{KPP} by a factor of 2-3 for the 50-level simulations and by an order of magnitude for the 200-level simulations. This enhancement is due to the large topographic slopes underneath the tracer, which induce large slopes of the s-levels, and the violation of the criterion $s_m < s_c$ (Equation 2) required to align the diffusive part of the advection scheme with isopycnal surfaces. This effect is confined to above the ridge as shown in Figures 8a and 8b. Note that the simulation whose tracer experiences the largest effective diffusivity is exp100-up3. Again, this illustrates the crucial role of rotating the upstream scheme to reduce spurious mixing.

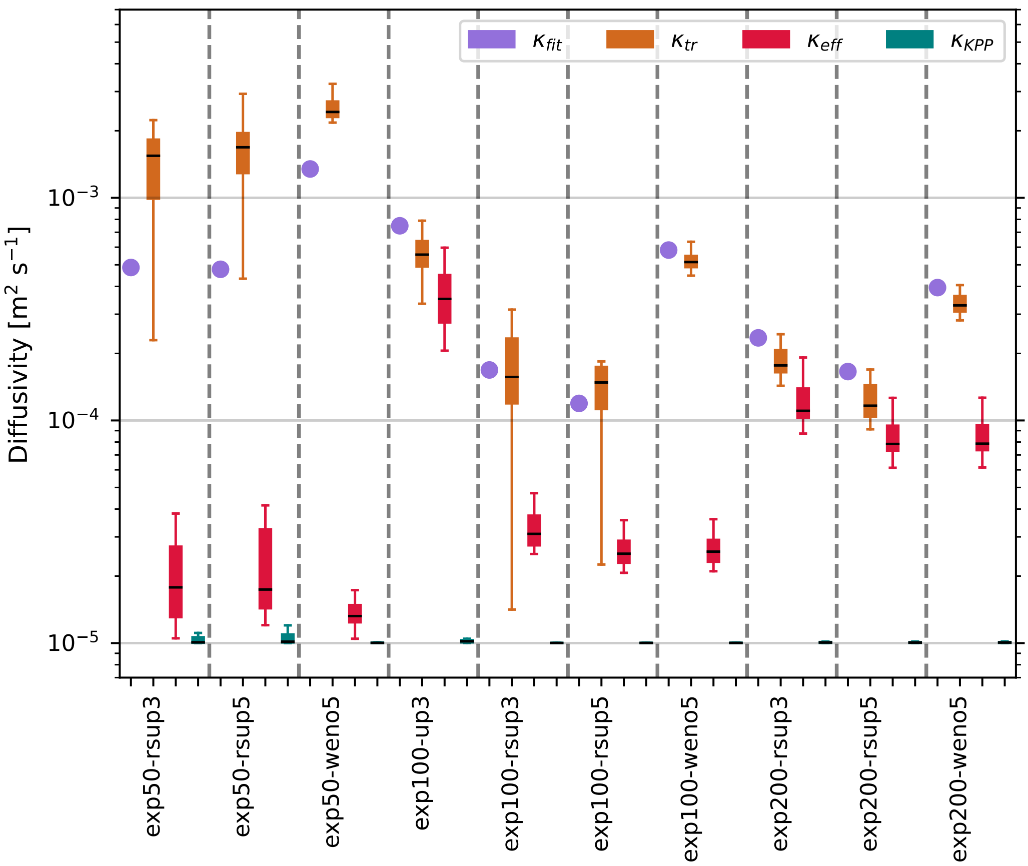

Figure 14. Same as Figure 13 but for tracer 2, released above the ridge.

Similar conclusions as for tracer 1 can be drawn for the tracer-based diapycnal diffusivities estimated for tracer 2. Specifically, for a given set of advection schemes, increasing the vertical resolution reduces the tracer-based diffusivity (Figure 14) until it reaches the effective mixing values. Using 50 levels is again too coarse for the fit method, and K_{fit} is much smaller than K_{tr}. However, with 100 and 200 levels, there is a good agreement between K_{fit} and K_{tr}. This, combined with the convergence of K_{tr} and K_{fit} towards K_{eff}, gives us confidence in the relevance of using TREs to diagnose mixing.

Among the different sets of schemes used, the weno5 combination is still more diffusive by a factor of 2 to 5 (depending on the vertical resolution) compared to rsup3 and rsup5. Among the upstream biased schemes, rsup5 is slightly less diffusive than rsup3, as expected.

Finally, note that K_{eff} should be very similar in the simulations using WENO5 and RSUP5 as the advection scheme for active tracers and momentum are the same. However, due to nonlinearities in the model, tracer patches slightly diverge across simulations, hence covers dynamically different regions. This results in small differences in tracer-based K_{eff} but their statistics are very similar.

3.6 Effect of smoothing topography

Since the most significant numerical mixing occurs over steep topographic slopes, one potential solution is to further smooth the original topography to reduce this effect. We tested this approach by applying a Gaussian smoothing kernel with a radius of 15 grid points, equivalent to three times the radius of the baseline bathymetry used in all other simulations. Using this smoothed topography, we conducted simulation exp200-rsup5-smooth, based on exp200-rsup5, which produced the largest numerical mixing over steep slopes.

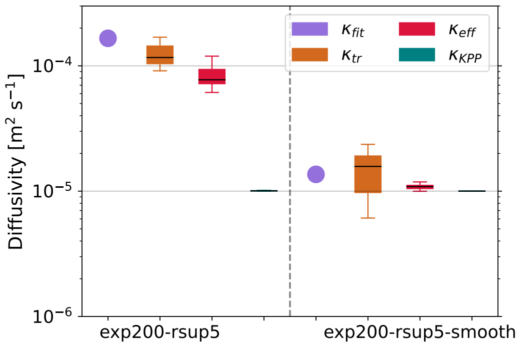

Figure 15. Diffusivities experienced by tracer 2 for configurations exp200-rsup5 and exp200-rsup5-smooth. The parameterised diffusivity K_{KPP} is in blue, the effective diffusivity K_{eff} is in red, and the two tracer-based diffusivities K_{tr} and K_{fit} are in orange and purple. K_{eff} and K_{KPP} are weighted by the tracer concentration following Equ. 14. Diffusivities are considered for the first 15 days. For each box plot, the extremities of the box represent the minimum and the maximum values of the distribution and the box shows the first quartile, the median and the third quartile of the distribution. K_{fit} is considered at 15 days.

The effect of increasing the smoothing can be seen directly in α_m and s_m, which are reduced over the steepest slopes of the ridge (Figures 8f and 8i). The fraction of grid points with $\alpha_m > \alpha_c$ and $s_m > s_c$ is significantly reduced. As a result, K_{eff} decreases and is much closer to the parameterised background value (Figure 8c).

The efficiency of smoothing the topography to reduce numerical mixing is well illustrated and quantified by the TRE of tracer 2 released over the ridge (Figure 15). In short, K_{eff}, K_{fit} and K_{tr} are all reduced by an order of magnitude and converge to K_{KPP}. Note that there is a physical effect of smoothing the topography that adds to the numerical effect, which is to reduce the energetic turbulence associated with flow-topography interactions. Indeed, reducing the topographic variance reduces the generation of internal tides (Garrett & Kunze, 2007) and also decreases the ratio of critical slopes where waves break (Lamb, 2014). Additionally, the slope Burger number of the modeled low-frequency flows would be reduced, hence they would be less prone to centrifugal and symmetric instabilities, both associated with irreversible mixing (Wenegrat et al., 2018; Gula et al., 2022). Thus, the isopycnal slopes above the ridge are reduced, which helps to reduce α_m.

4 Summary and Discussion

In this study, we investigated the diapycnal mixing in a realistic high-resolution simulation using a terrain-following coordinate model (CROCO) in a regional domain over the Reykjanes Ridge, including tides and high-frequency winds. In particular, we tested the impact of some numerical choices, namely, the tracer advection schemes and the vertical resolution, on the amount of numerical diapycnal mixing in the interior of the ocean.

We implemented two types of diagnostics to estimate the effective diapycnal mixing in the simulations, defined as the sum of the parameterized mixing and the numerical mixing. First, we implemented an online diagnostic, based on the computation of buoyancy fluxes across isopycnal surfaces at each time step of the model. In parallel, we tested an alternative and complementary method based on TREs (Holmes et al., 2019; Ruan & Ferrari, 2021). We used 10 configurations that differ in the horizontal and vertical advection schemes used and the number of vertical levels (Table 1). The results can be summarized as follows:

- Using standard numerical parameters for a submesoscale-permitting simulation ($\Delta x = 800$ m) over the Reykjanes Ridge, the dynamics do not generate significant mixing in the interior above steep topography via the Richardson-based parametrisation scheme, despite the intense internal wave activity. Vertical shear, mostly driven by internal waves, remains too small to trigger Richardson-based mixing. Therefore, the parameterized mixing is close to its background value in the interior over most of the domain and slightly weaker than the observed mixing. The parameterization fails to reproduce the contrast between the ridge and the abyssal plain, notably the intensified mixing in the lowest part of the water column above the ridge. Nonetheless, the effective mixing is enhanced above the ridge, which has a steeper seafloor topography. This led us to study these two regions separately.
- Over the abyssal plain, the effective mixing is close to the parameterized mixing, i.e., there is no significant numerical mixing despite the presence of internal waves. This is true for all experiments except for the one that uses the non-rotated upstream scheme UP3. This highlights the importance of using the isoneutral diffusive operator that is part of the horizontal advection scheme used for active tracers in the model. However, over the ridge, in the presence of steeper slopes, the effective mixing is an order of magnitude larger than the parameterized mixing when using standard numerical parameters and topography treatment, and therefore closer to observed in-situ values. This difference is explained in part by the presence of steep slopes, and in particular a grid slope ratio larger than 1, which limits the efficiency of the isoneutral diffusive operator.
- The numerical mixing can be greatly reduced by additional smoothing of the topography to ensure values of the grid slope ratio less than 1. In this case, the effective mixing is very close to the parameterized mixing over the entire domain.
- The tracer-based diffusivity estimates are much larger than the effective and parameterized mixing of the model at low vertical resolutions. Using 50 levels, the tracer-based diffusivities are two orders of magnitude larger than the effective mixing (10^{-3} m^2 s^{-1} vs 10^{-5} m^2 s^{-1}). This is explained either by dispersive effects in the vertical advection of the tracers when using a combination of RSUP3 and RSUP5 in the horizontal and SPLINES in the vertical, or by strong diffusive effects when using WENO5 schemes in the horizontal and vertical. Using 100 levels greatly reduces these effects and reduces tracer-based diffusivities by an order of magnitude. When 200 levels are used, the tracer-based diffusivity is further reduced, and converges to the effective diffusivity. Hence, we advocate for the use of (at least) 200 levels in similar regional setups to help reproducing tracer spreading correctly and reducing numerical mixing.
- We also find that WENO5 schemes are on average two to three times more diffusive than the combinations of RSUP3 and RSUP5 in the horizontal and SPLINES

in the vertical, regardless of the number of levels. But WENO5 schemes are, as expected, much more efficient to reduce oscillations and prevent negative tracer concentrations.

- Finally, the buoyancy-based diffusivity (K_{eff}) and the tracer-based diffusivities exhibit different behaviors when the vertical resolution increases. On the one hand, effective diffusivity increases with vertical resolution due to constraints on grid slopes. On the other hand, as it reflects both diffusive and dispersive processes, the tracer-based diffusivity decreases as dispersive errors decrease with an increase in vertical resolution. Ultimately, the tracer-based diffusivities converge on the buoyancy-based diffusivity when dispersive effects are no longer significant.

An important issue is the realism of mixing in the simulation. The KPP parameterization tends to underestimate the diffusivity over the ridge, raising the question of whether this deficiency is due to the resolution of the model or to deficiencies in the vertical mixing parameterization. Within the KPP framework, this could potentially be addressed by adjusting the background diffusivity or Richardson number-based mixing, as suggested in Thakur et al. (2022) and Momeni et al. (2024). However, more detailed resolution sensitivity studies and comparisons with in-situ observations (including vertical shear) would be needed to confirm whether the same method can be applied with a different model and in a different region.

The numerical mixing, which tends to exceed the parameterized mixing on steep slopes, is fortuitously more consistent with in-situ observations and adds realism to the simulation in this particular case. This numerical mixing results from discretization errors and implicit advective diffusion that partially compensate for the limitations of explicit parameterizations. While some degree of numerical mixing can be beneficial, it poses a challenge because it cannot be directly controlled. Therefore, it is important to evaluate and monitor it for a specific model setup and configuration to ensure that it remains within realistic bounds.

Reducing, or at least controlling, numerical mixing in global and regional ocean models has been a major concern of the community (e.g., Griffies et al., 2000; Burchard & Rennau, 2008; Marchesiello et al., 2009; Hill et al., 2012). Our study shows that it might involve dilemmas. While increasing the vertical resolution actually reduces dispersive and/or diffusive effects related to the vertical advection and leads to a more realistic representation of tracers, it can also increase numerical mixing by increasing the grid slope ratio beyond acceptable limits, which renders the isoneutral diffusive operator less effective. Thus, if limiting the numerical mixing to values less than the parameterized mixing in the interior of the ocean is a priority, e.g. when performing long-term equilibration or studying water mass transformation, one must be very careful in controlling the numerical mixing.

A first obvious solution is to further smooth the topography to ensure that the grid slope ratio remains of order one most of the time. It is not possible to compute the grid slope ratio a priori, without knowledge of the isopycnal slopes. However, this is largely achieved in practice by keeping the hydrostatic consistency condition rx_1 (Haney, 1991) close to unity for most of the domain (Figure 9g,h,i). Although not thoroughly diagnosed in the simulations, we anticipate that the downside of the additional smoothing of the seafloor topography would also change the flow-topography interactions. For example, small-scale topographic features are important for converting barotropic tides into high-mode internal waves (Melet et al., 2013) or for generating submesoscale instabilities (Gula et al., 2016).

A better short-term solution might be to work on a new version of the isoneutral mixing operator currently implemented in CROCO. Since the current implementation of the isoneutral mixing operator was designed under the small-slope approximation (Lemarié et al., 2012a), one could think about a finite-slope version that is able to handle the topographic gradients encountered in the high-resolution simulations used here. Other promising solutions to these problems could be the incorporation of small-scale topography via penalization methods such as the Brinkman penalization approach (Debreu et al., 2020, 2022) or the Multi-Envelope method (Bruciaferri et al., 2018, 2024; Wise et al., 2022), which allows to account for steep topographic slopes without increasing the grid-slope ratio excessively. In the long run, the use of a generalized vertical coordinate formulation with Arbitrary Lagrangian-Eulerian or Vertical Lagrangian Remap methods should provide another efficient way to minimise spurious mixing (Klingbeil et al., 2019; Griffies et al., 2020).

Although WENO5 schemes are generally more diffusive than other combinations, they are excellent at preventing oscillations and negative tracer concentrations. Therefore, they are essential when monotonicity is a strict requirement, as with biogeochemical tracers. However, the excessive diapycnal diffusion observed here is not inherent to the WENO scheme itself, but results from the fact that it does not benefit from isoneutral rotation of the diffusion terms, as the RSUP3/5 schemes do. Thus, implementing some form of isoneutral rotation may be a solution to avoid excessive diapycnal mixing while remaining essentially monotonic. This could also be improved by increasing the order of the scheme to 7th or 9th order WENO schemes.

Finally, this study did not directly investigate the impact of horizontal resolution on numerical mixing in our set of simulations. However, since the main limiting criteria are the isopycnal slope α_m and the grid slope ratio s_m, the question is how the horizontal resolution modifies these values. Increasing the horizontal resolution while keeping the other parameters (topographic/buoyancy slopes and vertical resolution) constant will decrease the values of both parameters in the model and help reduce spurious diapycnal effects. However, the answer becomes less obvious if the topographic slopes and/or the vertical resolution increase alongside the horizontal resolution, or if changes in the dynamics result in larger isopycnal slopes.

Appendix A Horizontal pressure gradient errors

Another important issue when using terrain-following models is the accuracy of the computation of the horizontal pressure gradients, as errors can appear over topographic slopes due to the misalignment of the vertical coordinate with the geopotential (e.g., Haney, 1991; Beckmann & Haidvogel, 1993b).

We estimated the horizontal pressure gradient errors in our configurations by performing experiments that started from a resting state, following the classical experiments described in Haidvogel and Beckmann (1999). The configurations are identical to those used here in terms of numerics, except that they do not include any forcing or explicit diffusion, and the initial state is at rest. The stratification was constructed by averaging the temperature and salinity horizontally in the realistic configuration (Fig. A2a).

Figure A2 shows the evolution of the maximum and volume-averaged velocities for 3 configurations over 180 days, which is much longer than the typical duration of the simulations used here. The configurations include one of the realistic experiments (exp100-rsup3) used in the article, as well as a configuration starting from a resting state (exp100-rsup3-rest) and a configuration using the smoothed bathymetry (exp100-rsup3-smooth-rest).

These simulations highlight that the currents generated in the last two cases remain small compared to the realistic case, especially with the smoothed bathymetry. The maximum velocity error is 2 cm s^{-1} with the standard bathymetry and 1 cm s^{-1} with the smoothed bathymetry. The maximum error is reached within a month with the standard bathymetry, whereas it takes around three months with the smoothed bathymetry. After the initial stage where velocities increase, the maximum velocity remains constant

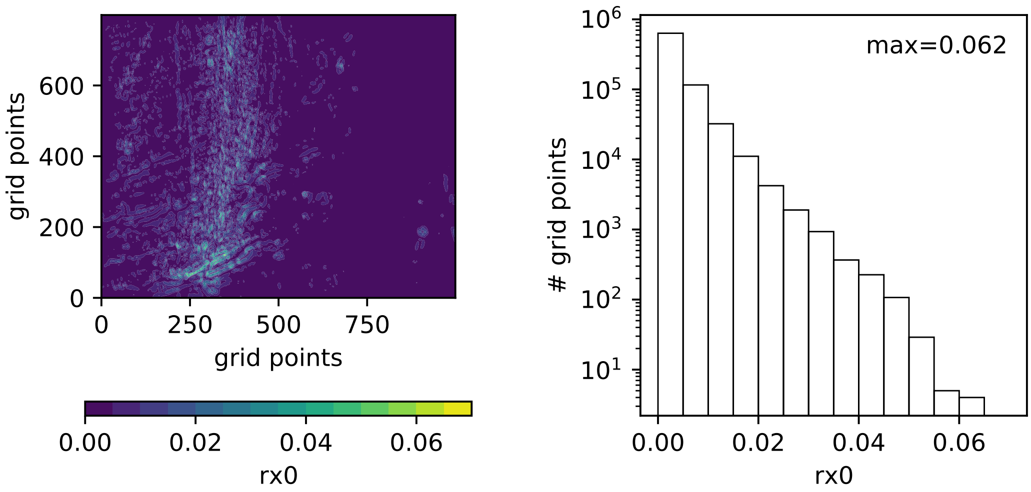

Figure A1. Parameter rx_0 (left) on the model grid and (right) its histogram.

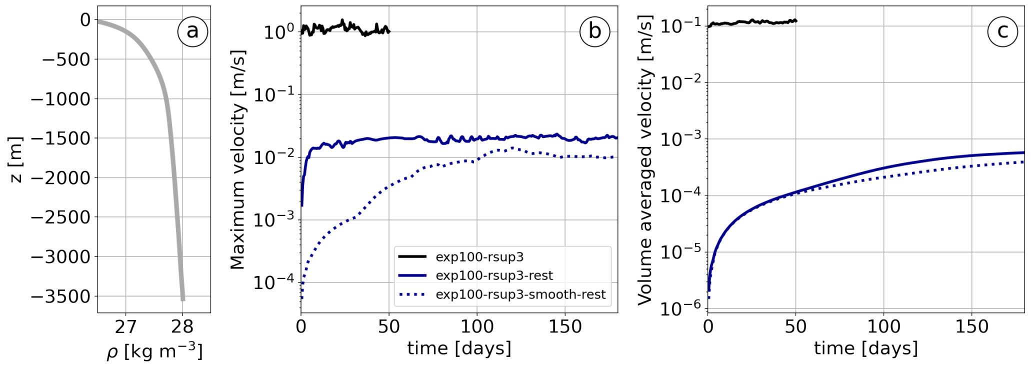

Figure A2. (a) Horizontally averaged model initial potential density; (b) maximum velocity; and (c) volume-averaged velocity for the realistic configuration (exp100-rsup3) and resting state (exp100-rsup3-rest) experiments, using the same setup, and for the resting state (exp100-rsup3-smooth-rest) experiment, using smoothed bathymetry.

over longer timescales because the model has reached a state of balance, with the frictional effects offsetting the growth of the error. These values are consistent with those of other recent studies examining horizontal pressure gradient errors (e.g., Bruciaferri et al., 2018; Wise et al., 2022; Bruciaferri et al., 2024).

As expected, the largest amplitudes are found on the largest topographic slopes, as shown in Fig. A3. The map of the bottom currents after two months of simulation (identical to the duration of the realistic simulations used in the article) shows that the currents appear in the resting state experiments in specific regions of the ridge, particularly in the Bight Fracture Zone at ≈57°N, which features the largest slopes of the domain (Fig. A1). The distribution of the currents against the steepness parameter rx_0 and the hydrostatic consistency condition rx_1 confirms the relationship between the two (Figure A3).

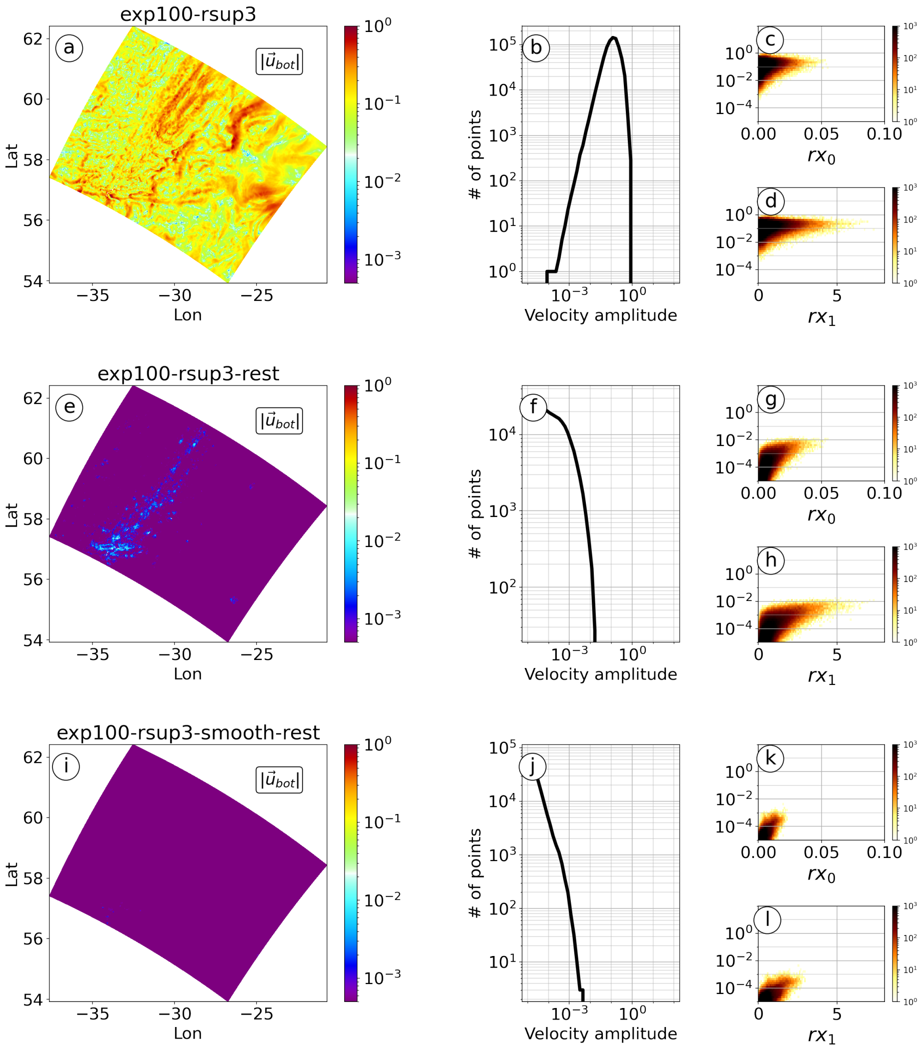

Figure A3. (a,e,i) Map and (b,f,j) distribution of bottom velocity amplitude (at 50 m above bottom) after 60 days of simulation for exp100-rsup3, exp100-rsup3-rest and exp100-rsup3-smooth-rest. Binned histograms for the bottom velocity amplitude versus the steepness parameter rx_0 (c,g,k) and the hydrostatic consistency condition rx_1 (d,h,l).

Appendix B Test with an isoneutral slope temporal filter and a centered advective scheme (C4)

Here we present some additional tests we performed. We compare the exp100-rsup3 configuration presented above with two additional configurations:

- exp100-rsup3-filt, which is the same configuration as exp100-rsup3 with an additional temporal filter that modifies the isoneutral slopes. This filter is activated by the TS_MIX_ISO_FILT key in CROCO. It is an exponential smoothing with a time scale of 1 day;
- exp100-c4, which uses a fourth-order centered advective scheme (C4) for the horizontal advection of the tracers, with no additional diffusivity added. The rest of the configuration is identical to exp100-rsup3.

The time filter in exp100-rsup3-filt, activated via TS_MIX_ISO_FILT, is a default choice in CROCO. For configurations introduced in Table 1, the key TS_MIX_ISO_FILT is not activated. No evidence for numerical instabilities related to isoneutral diffusion was found when the time filter was not used. However the time filter leads to a noticeable increase in the numerical diffusivity, even with a time scale as small as 1 day (the default value in CROCO). We see that the effective mixing increases by a factor of 3 to 5 over the abyssal plain and the ridge (Fig. B1). The 1-day time scale is large enough to suppress isopycnal oscillations due to high-frequency processes. We also tested a time scale of 3 hours (not shown) and still observed an increase in effective diffusivity compared to the case with no time filtering.

The use of a centered advective scheme for tracer advection without diffusivity would be considered a bad numerical practice, as it is expected to lead to strong dispersive errors. This is exactly what we observe in Figure B1. The tracer-based diffusivities are much higher than for any other configuration, leading to a much larger dispersion of the tracer cloud and extra diapycnal diffusivities. Above the abyssal plain, the effective diffusivity is very small because the method does not take into account dispersive effects. Above the ridge, the effective mixing is stronger in exp100-c4 compared to exp100-rsup3 only because the tracer penetrates inside the bottom boundary layer.

Appendix C Details about the one-dimensional method K_{fit}

Here, we demonstrate that the one-dimensional method from Holmes et al. (2019) used to compute K_{fit} is contingent upon the vertical resolution of the simulation. Figure C1 shows how the concentration of tracer 1 evolves over time when it is binned in buoyancy space using configurations exp50-rsup5 and exp200-rsup5. When 50 s-levels are used, the one-dimensional fit of the three-dimensional tracer concentration binned in buoyancy space does not accurately represent the distribution. Conversely, when 200 s-levels are used, the one-dimensional fit improves. Therefore, 50 s-levels do not provide sufficient vertical resolution of the tracer to obtain a robust estimate of K_{fit}.

Data Availability Statement

Information about GIGATL3 and how to access the data can be found at (Gula et al., 2021) (`https://doi.org/10.5281/zenodo.4948523`). The Python code and NetCDF files containing the diapycnal diffusivities experienced by the tracer patches used to create the figures in this study can be downloaded from Schifano (2025) (`https://doi.org/https:/doi.org/10.5281/zenodo.15496614`) to recreate the figures. The version of the CROCO code used in this article can be found in *Version of the CROCO code used.* (2025) (`https://doi.org/10.5281/zenodo.15496858`), that is adapted from Auclair et al. (2022). The file "set_diags_pv.F" contains the diagnostic of K_{eff}. Microstructure dataset from

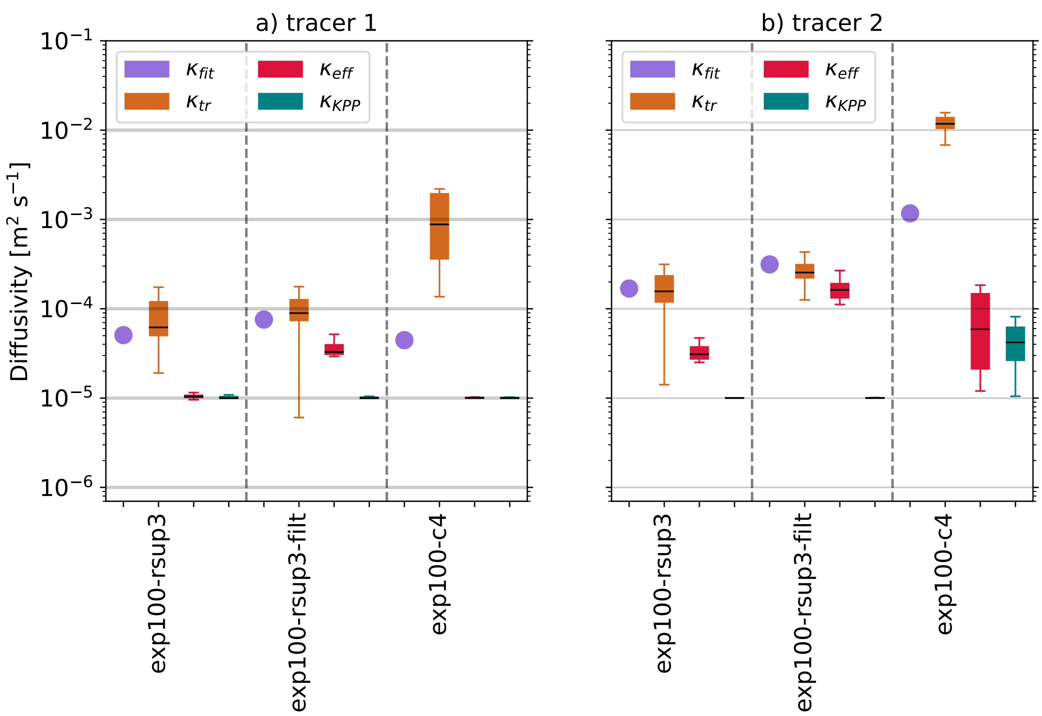

Figure B1. Estimation of the diffusivities experienced by a) tracer 1 and b) tracer 2 for configurations exp100-rsup3, exp100-rsup3-filt and exp100-c4. The parameterised diffusivity is shown in blue, the effective diffusivity K_{eff} is in red, and the two tracer-based diffusivities K_{tr} and K_{fit} are in orange and purple. K_{eff} and K_{KPP} are weighted by the tracer concentration following Equ. 14. Diffusivities are considered for the first 15 days. For each box plot, the extremities of the box represent the minimum and the maximum values of the distribution and the box shows the first quartile, the median and the third quartile of the distribution. K_{fit} is considered over the last 10 days.

the OVIDE A25 2008 cruise (2024-09-16), doi: 10.17882/101925 (Ferron et al., 2008). Microstructure dataset from the Reykjanes Ridge Experiment (RREX) 2015 cruise (2024-09-16), doi: 10.17882/10193 (Ferron et al., 2015). Microstructure dataset from the Reykjanes Ridge Experiment (RREX) 2017 cruise (2024-09-16), doi: 10.17882/101939 (Ferron et al., 2017).

Acknowledgments

The authors would like to acknowledge Bruno Ferron for sharing the in-situ data from campaigns RREX15, RREX17 and OVIDE08. We thank all crew members of R/V Thalassa and Atalante and Virginie Thierry for her contribution to the organization of the RREX cruises. We also thank Michel Hamon, Brian Hogues, Stéphane Leizour, Olivier Ménage, and Olivier Peden for their technical assistance with the VMP cruise operations and data processing. The microstructure profilers were funded by the French Agence Nationale de la Recherche (ANR) through grant ANR-JC05_50690 and by the French Institute for Marine Science (IFREMER). We would also like to thank Ryan Holmes for sharing his code to compute the diffusivities K_{fit}, Patrick Marchesiello for numerous discussions about numerical options in CROCO, and Henri Drake, Xiaozhou Ruan and Raffaele Ferrari for the discussions about the TREs. The authors would also like to acknowledge the reviewers for their helpful comments.

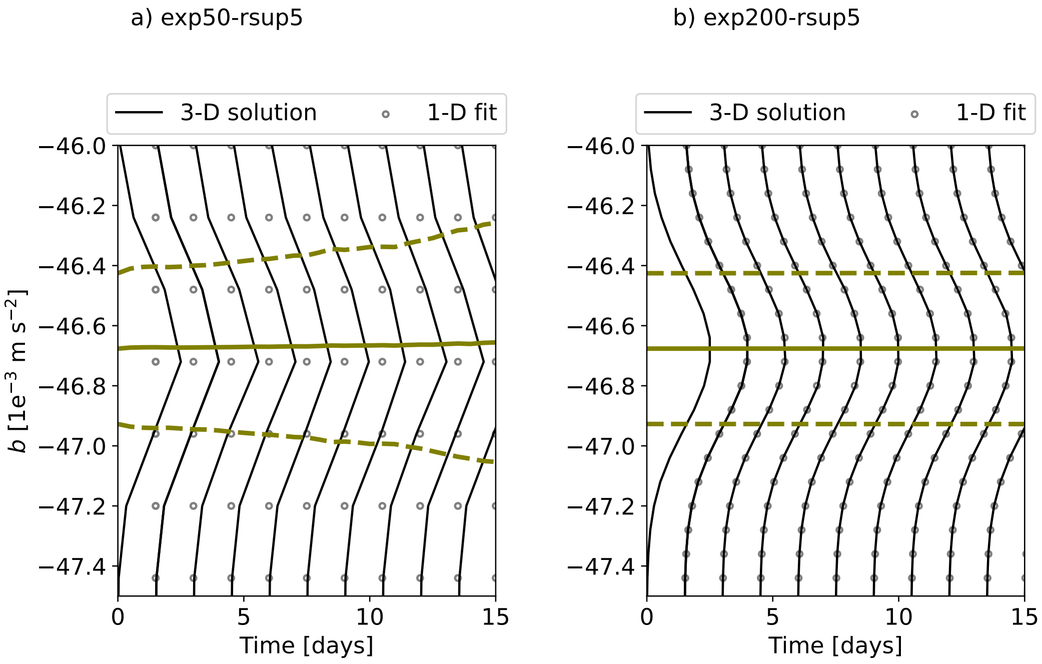

Figure C1. a,b) tracer 1 concentration binned in buoyancy space (black line) and one-dimensional fit used to compute K_{fit} (dot markers) for configurations a) exp50-rsup5 and b) exp200-rsup5. Green lines show the center of gravity (plain) and the standard deviation (dashed) for the one-dimensional fit (equation 15).

This work was supported by the French National Agency for Research (ANR) through the project DEEPER (ANR-19-CE01-0002-01), by the Office of Naval Research (ONR grant N00014-23-1-2226), and by the Interdisciplinary Graduate School for the Blue Planet project (ANR-17-EURE-0015). Simulations were performed using HPC resources from GENCI-TGCC (Grants 2024-A0170112051), and from HPC facilities DATARMOR of "Pôle de Calcul Intensif pour la Mer" at Ifremer Brest France.

References

Alford, M. H. (2020). Global calculations of local and remote near-inertial-wave dissipation. *Journal of Physical Oceanography*, *50*(11), 3157–3164. doi: 10.1175/JPO-D-20-0106.1

Alford, M. H., MacKinnon, J. A., Simmons, H. L., & Nash, J. D. (2016). Near-inertial internal gravity waves in the ocean. *Annu. Rev. Mar. Sci.*, *8*, 95–123. doi: 10.1146/annurev-marine-010814-015746

Arbic, B. K. (2022). Incorporating tides and internal gravity waves within global ocean general circulation models: A review. *Progress in Oceanography*, 102824. doi: 10.1016/j.pocean.2022.102824

Arbic, B. K., Wallcraft, A. J., & Metzger, E. J. (2010). Concurrent simulation of the eddying general circulation and tides in a global ocean model. *Ocean Modelling*, *32*(3-4), 175–187. doi: 10.1016/j.ocemod.2010.01.007

Auclair, F., Benshila, R., Bordois, L., Boutet, M., Brémond, M., Caillaud, M., … Theetten, S. (2022, December). *Coastal and regional ocean community model.* Zenodo. Retrieved from `https://doi.org/10.5281/zenodo.7415343` doi: 10.5281/zenodo.7415343

Baker, L., Mashayek, A., & Naveira Garabato, A. (2023). Boundary upwelling of Antarctic Bottom Water by topographic turbulence. *AGU Advances*, *4*(5), e2022AV000858. doi: 10.1029/2022AV000858

Banerjee, T., Danilov, S., Klingbeil, K., & Campin, J.-M. (2024). Discrete variance decay analysis of spurious mixing. *Ocean Modelling*, *192*, 102460.

Barkan, R., Srinivasan, K., Yang, L., McWilliams, J. C., Gula, J., & Vic, C. (2021a). Oceanic mesoscale eddy depletion catalyzed by internal waves. *Geophysical Research Letters*, *48*(18), e2021GL094376. doi: 10.1029/2021GL094376

Barkan, R., Srinivasan, K., Yang, L., McWilliams, J. C., Gula, J., & Vic, C. (2021b). Oceanic mesoscale eddy depletion catalyzed by internal waves. *Geophysical Research Letters*, *48*(18), e2021GL094376. Retrieved from `https://agupubs.onlinelibrary.wiley.com/doi/abs/10.1029/2021GL094376` (e2021GL094376 2021GL094376) doi: https://doi.org/10.1029/2021GL094376

Beckmann, A., & Haidvogel, D. B. (1993a). Numerical simulation of flow around a tall isolated seamount. Part I: Problem formulation and model accuracy. *J. Phys. Oceanogr.*, *23*(8), 1736–1753. doi: 10.1175/1520-0485(1993)023⟨1736:NSOFAA⟩2.0.CO;2

Beckmann, A., & Haidvogel, D. B. (1993b). Numerical simulation of flow around a tall isolated seamount. part i: Problem formulation and model accuracy. *Journal of Physical Oceanography*, *23*(8), 1736–1753.

Boyd, J. P. (1994). Hyperviscous shock layers and diffusion zones: Monotonicity, spectral viscosity, and pseudospectral methods for very high order differential equations. *Journal of Scientific Computing*, *9*, 81–106.

Bracco, A., Choi, J., Kurian, J., & Chang, P. (2018). Vertical and horizontal resolution dependency in the model representation of tracer dispersion along the continental slope in the northern gulf of mexico. *Ocean Modelling*, *122*, 13–25. doi: https://doi.org/10.1016/j.ocemod.2017.12.008

Branellec, P., & Thierry, V. (2016). Rrex 2015. ctd-o2 data report.

Branellec, P., & Thierry, V. (2018). *Rrex 2017. ctd-o2 data report, rap. int* (Tech. Rep.). LOPS/18-04, https://doi. org/10.13155/58074.

Bruciaferri, D., Guiavarc'h, C., Hewitt, H. T., Harle, J., Almansi, M., Mathiot, P., & Colombo, P. (2024). Localized general vertical coordinates for quasi-Eulerian ocean models: The Nordic overflows test-case. *Journal of Advances in Modeling Earth Systems*, *16*(3), e2023MS003893.

Bruciaferri, D., Shapiro, G. I., & Wobus, F. (2018). A multi-envelope vertical coordinate system for numerical ocean modelling. *Ocean Dynamics*, *68*, 1239–1258.

Burchard, H., Craig, P. D., Gemmrich, J. R., van Haren, H., Mathieu, P.-P., Meier, H. M., … others (2008). Observational and numerical modeling methods for quantifying coastal ocean turbulence and mixing. *Progress in oceanography*, *76*(4), 399–442.

Burchard, H., Gräwe, U., Klingbeil, K., Koganti, N., Lange, X., & Lorenz, M. (2021). Effective diahaline diffusivities in estuaries. *Journal of Advances in Modeling Earth Systems*, *13*(2).

Burchard, H., & Rennau, H. (2008). Comparative quantification of physically and numerically induced mixing in ocean models. *Ocean Modelling*, *20*(3), 293–311. doi: 10.1016/j.ocemod.2007.10.003

Capó, E., McWilliams, J. C., Gula, J., Molemaker, M. J., Damien, P., & Schubert, R. (2024). Abyssal slope currents. *Journal of Physical Oceanography*, *54*(11), 2373 - 2392. Retrieved from `https://journals.ametsoc.org/view/journals/phoc/54/11/JPO-D-24-0028.1.xml` doi: 10.1175/JPO-D-24-0028.1

Debreu, L., Kevlahan, N.-R., & Marchesiello, P. (2020). Brinkman volume penalization for bathymetry in three-dimensional ocean models. *Ocean Modelling*, *145*, 101530. Retrieved from `https://www.sciencedirect.com/science/article/pii/S146350031930174X` doi: https://doi.org/10.1016/j.ocemod.2019.101530

Debreu, L., Kevlahan, N.-R., & Marchesiello, P. (2022). Improved gulf stream separation through brinkman penalization. *Ocean Modelling*, *179*, 102121. Retrieved from https://www.sciencedirect.com/science/article/pii/S1463500322001354 doi: https://doi.org/10.1016/j.ocemod.2022.102121

de Lavergne, C., Falahat, S., Madec, G., Roquet, F., Nycander, J., & Vic, C. (2019). Toward global maps of internal tide energy sinks. *Ocean Modell.*, *137*, 52–75. doi: 10.1016/j.ocemod.2019.03.010

de Lavergne, C., Groeskamp, S., Zika, J., & Johnson, H. L. (2022). The role of mixing in the large-scale ocean circulation. In *Ocean mixing* (pp. 35–63). Elsevier. doi: https://doi.org/10.1016/B978-0-12-821512-8.00010-4

de Lavergne, C., Vic, C., Madec, G., Roquet, F., Waterhouse, A., Whalen, C., … Hibiya, T. (2020). A parameterization of local and remote tidal mixing. *Journal of Advances in Modeling Earth Systems*, *12*(5). doi: 10.1029/2020MS002065

Delpech, A., Barkan, R., Srinivasan, K., McWilliams, J. C., Arbic, B. K., Siyanbola, O. Q., & Buijsman, M. C. (2024). Eddy–internal wave interactions and their contribution to cross-scale energy fluxes: A case study in the California current. *Journal of Physical Oceanography*, *54*(3), 741–754.

Drake, H. F., Bailey, S., Dussin, R., Griffies, S. M., Krasting, J., MacGilchrist, G., … Zika, J. D. (2025). Water mass transformation budgets in finite-volume generalized vertical coordinate ocean models. *Journal of Advances in Modeling Earth Systems*, *17*(3), e2024MS004383.

Ferron, B., Cortes, N., & Mercier, H. (2008). *Microstructure dataset from the ovide a25 2008 cruise* [Dataset]. Retrieved from https://doi.org/10.17882/101925 doi: 10.17882/101925

Ferron, B., Hamon, M., Hogue, B., Peden, O., & Thierry, V. (2017). *Microstructure dataset from the reykjanes ridge experiment (rrex) 2017 cruise* [Dataset]. Retrieved from https://doi.org/10.17882/101939 doi: 10.17882/101939

Ferron, B., Hamon, M., Leizour, S., Menage, O., & Thierry, V. (2015). *Microstructure dataset from the reykjanes ridge experiment (rrex) 2015 cruise* [Dataset]. Retrieved from https://doi.org/10.17882/101935 doi: 10.17882/101935

Ferron, B., Kokoszka, F., Mercier, H., & Lherminier, P. (2014). Dissipation rate estimates from microstructure and finescale internal wave observations along the A25 Greenland–Portugal OVIDE line. *Journal of Atmospheric and Oceanic Technology*, *31*(11), 2530–2543.

Frajka-Williams, E., Brearley, J. A., Nash, J. D., & Whalen, C. B. (2022). New technological frontiers in ocean mixing. In *Ocean mixing* (pp. 345–361). Elsevier.

Garrett, C., & Kunze, E. (2007). Internal tide generation in the deep ocean. *Annu. Rev. Fluid Mech.*, *39*, 57–87. doi: https://doi.org/10.1146/annurev.fluid.39.050905.110227

Getzlaff, J., Nurser, G., & Oschlies, A. (2010). Diagnostics of diapycnal diffusivity in z-level ocean models part i: 1-dimensional case studies. *Ocean Modelling*, *35*(3), 173–186.

Getzlaff, J., Nurser, G., & Oschlies, A. (2012). Diagnostics of diapycnal diffusion in z-level ocean models. Part II: 3-dimensional OGCM. *Ocean Modelling*, *45*, 27–36.

Gregg, M. C., D'Asaro, E. A., Riley, J. J., & Kunze, E. (2018). Mixing efficiency in the ocean. *Annual review of marine science*, *10*(1), 443–473.

Griffies, S. M., Adcroft, A., & Hallberg, R. W. (2020). A primer on the vertical lagrangian-remap method in ocean models based on finite volume generalized vertical coordinates. *Journal of Advances in Modeling Earth Systems*, *12*(10), e2019MS001954. Retrieved from https://agupubs.onlinelibrary.wiley.com/doi/abs/10.1029/2019MS001954 (e2019MS001954 10.1029/2019MS001954) doi: https://doi.org/10.1029/2019MS001954

Griffies, S. M., Gnanadesikan, A., Pacanowski, R. C., Larichev, V. D., Dukowicz, J. K., & Smith, R. D. (1998). Isoneutral diffusion in a z-coordinate ocean model. *Journal of Physical Oceanography*, *28*(5), 805 - 830. Retrieved from `https://journals.ametsoc.org/view/journals/phoc/28/5/1520-0485_1998_028_0805_idiazc_2.0.co_2.xml` doi: 10.1175/1520-0485(1998)028⟨0805:IDIAZC⟩2.0.CO;2

Griffies, S. M., & Hallberg, R. W. (2000). Biharmonic friction with a smagorinsky-like viscosity for use in large-scale eddy-permitting ocean models. *Monthly Weather Review*, *128*(8), 2935 - 2946. Retrieved from `https://journals.ametsoc.org/view/journals/mwre/128/8/1520-0493_2000_128_2935_bfwasl_2.0.co_2.xml` doi: 10.1175/1520-0493(2000)128⟨2935:BFWASL⟩2.0.CO;2

Griffies, S. M., Pacanowski, R. C., & Hallberg, R. W. (2000). Spurious diapycnal mixing associated with advection in a z-coordinate ocean model. *Monthly Weather Review*, *128*(3), 538–564. doi: https://doi.org/10.1175/1520-0493(2000)128⟨0538:SDMAWA⟩2.0.CO;2

Gula, J., Blacic, T. M., & Todd, R. E. (2019). Submesoscale coherent vortices in the Gulf Stream. *Geophysical Research Letters*, *46*(5), 2704–2714. doi: 10.1029/2019GL081919

Gula, J., Molemaker, M. J., & McWilliams, J. C. (2016). Topographic generation of submesoscale centrifugal instability and energy dissipation. *Nat. Commun.*, *7*. doi: 10.1038/ncomms12811

Gula, J., Taylor, J., Shcherbina, A., & Mahadevan, A. (2022). Submesoscale processes and mixing. In *Ocean mixing* (pp. 181–214). Elsevier.

Gula, J., Theetten, S., Cambon, G., & Roullet, G. (2021, June). *Description of the gigatl simulations.* Zenodo. Retrieved from `https://doi.org/10.5281/zenodo.4948523` doi: 10.5281/zenodo.4948523

Haidvogel, D. B., & Beckmann, A. (1999). *Numerical ocean circulation modeling* (Vol. 344). Imperial College Press London.

Haney, R. L. (1991). On the pressure gradient force over steep topography in sigma coordinate ocean models. *Journal of Physical Oceanography*, *21*(4), 610 - 619. Retrieved from `https://journals.ametsoc.org/view/journals/phoc/21/4/1520-0485_1991_021_0610_otpgfo_2_0_co_2.xml` doi: 10.1175/1520-0485(1991)021⟨0610:OTPGFO⟩2.0.CO;2

Hecht, M. W. (2010). Cautionary tales of persistent accumulation of numerical error: Dispersive centered advection. *Ocean Modelling*, *35*(3), 270–276. doi: 10.1016/j.ocemod.2010.07.005

Hill, C., Ferreira, D., Campin, J.-M., Marshall, J., Abernathey, R., & Barrier, N. (2012). Controlling spurious diapycnal mixing in eddy-resolving height-coordinate ocean models–insights from virtual deliberate tracer release experiments. *Ocean Modelling*, *45*, 14–26. doi: 10.1016/j.ocemod.2011.12.001

Hofmann, M., & Morales Maqueda, M. (2006). Performance of a second-order moments advection scheme in an ocean general circulation model. *Journal of Geophysical Research: Oceans*, *111*(C5). doi: https://doi.org/10.1029/2005JC003279

Holmes, R. M., de Lavergne, C., & Mcdougall, T. J. (2019). Tracer transport within abyssal mixing layers. *Journal of Physical Oceanography*, *49*(10), 2669–2695. doi: https://doi.org/10.1175/JPO-D-19-0006.1

Ilıcak, M., Adcroft, A. J., Griffies, S. M., & Hallberg, R. W. (2012). Spurious dianeutral mixing and the role of momentum closure. *Ocean Modelling*, *45*, 37–58. doi: 10.1016/j.ocemod.2011.10.003

Jackett, D., & McDougall, T. (1995). Minimal adjustment of hydrographic profiles to achieve static stability. *J. Atmos. Oceanic Technol.*, *12*(2), 381–389.

Jayne, S. R., & St Laurent, L. C. (2001). Parameterizing tidal dissipation over rough topography. *Geophysical Research Letters*, *28*(5), 811–814. doi: 10.1029/

2000GL012044

Jiang, G.-S., & Shu, C.-W. (1996). Efficient implementation of weighted eno schemes. *Journal of Computational Physics*, *126*(1), 202-228. Retrieved from https://www.sciencedirect.com/science/article/pii/S0021999196901308 doi: https://doi.org/10.1006/jcph.1996.0130

Jiménez, J. (1994). Hyperviscous vortices. *Journal of Fluid Mechanics*, *279*, 169–176.

Klingbeil, K., Burchard, H., Danilov, S., Goetz, C., & Iske, A. (2019). Reducing spurious diapycnal mixing in ocean models. In C. Eden & A. Iske (Eds.), *Energy transfers in atmosphere and ocean* (pp. 245–286). Cham: Springer International Publishing. Retrieved from https://doi.org/10.1007/978-3-030-05704-6_8 doi: 10.1007/978-3-030-05704-6_8

Klingbeil, K., Mohammadi-Aragh, M., Gräwe, U., & Burchard, H. (2014). Quantification of spurious dissipation and mixing – discrete variance decay in a finite-volume framework. *Ocean Modelling*, *81*, 49-64. Retrieved from https://www.sciencedirect.com/science/article/pii/S1463500314000754 doi: https://doi.org/10.1016/j.ocemod.2014.06.001

Kunze, E., Firing, E., Hummon, J. M., Chereskin, T. K., & Thurnherr, A. M. (2006). Global abyssal mixing inferred from lowered adcp shear and ctd strain profiles. *Journal of Physical Oceanography*, *36*(8), 1553–1576. doi: https://doi.org/10.1175/JPO2926.1

Lamb, K. G. (2014). Internal wave breaking and dissipation mechanisms on the continental slope/shelf. *Annual Review of Fluid Mechanics*, *46*(1), 231–254.

Large, W. G., McWilliams, J. C., & Doney, S. C. (1994). Oceanic vertical mixing: A review and a model with a nonlocal boundary layer parameterization. *Reviews of geophysics*, *32*(4), 363–403. doi: https://doi.org/10.1029/94RG01872

Le Corre, M., Gula, J., & Tréguier, A.-M. (2020). Barotropic vorticity balance of the North Atlantic subpolar gyre in an eddy-resolving model. *Ocean Science*, *16*(2), 451–468. doi: 10.5194/os-16-451-2020

Ledwell, J. R., Montgomery, E., Polzin, K., St Laurent, L., Schmitt, R., & Toole, J. (2000). Evidence for enhanced mixing over rough topography in the abyssal ocean. *Nature*, *403*(6766), 179–182.

Ledwell, J. R., & Watson, A. J. (1991). The santa monica basin tracer experiment: A study of diapycnal and isopycnal mixing. *Journal of Geophysical Research: Oceans*, *96*(C5), 8695–8718.

Ledwell, J. R., Watson, A. J., & Law, C. S. (1993). Evidence for slow mixing across the pycnocline from an open-ocean tracer-release experiment. *Nature*, *364*(6439), 701–703.

Lee, M.-M., Coward, A. C., & Nurser, A. G. (2002). Spurious diapycnal mixing of the deep waters in an eddy-permitting global ocean model. *Journal of physical oceanography*, *32*(5), 1522–1535.

Lemarié, F., Debreu, L., Shchepetkin, A., & Mcwilliams, J. C. (2012a). On the stability and accuracy of the harmonic and biharmonic isoneutral mixing operators in ocean models. *Ocean Modell.*, *52*, 9–35. doi: 10.1016/j.ocemod.2012.04.007

Lemarié, F., Debreu, L., Shchepetkin, A., & Mcwilliams, J. C. (2012b). On the stability and accuracy of the harmonic and biharmonic isoneutral mixing operators in ocean models. *Ocean Modell.*, *52*, 9–35. doi: 10.1016/j.ocemod.2012.04.007

Marchesiello, P., Debreu, L., & Couvelard, X. (2009). Spurious diapycnal mixing in terrain-following coordinate models: The problem and a solution. *Ocean Modelling*, *26*(3-4), 156–169. doi: 10.1016/j.ocemod.2008.09.004

Marchesiello, P., McWilliams, J., & Shchepetkin, A. (2003). Equilibrium structure and dynamics of the California Current System. *J. Phys. Oceanogr.*, *33*(4), 753–783. doi: 10.1175/1520-0485(2003)33⟨753:ESADOT⟩2.0.CO;2

Mashayek, A., Gula, J., Baker, L. E., Garabato, A. C. N., Cimoli, L., Riley, J. J., & de Lavergne, C. (2024). On the role of seamounts in upwelling deep-ocean waters through turbulent mixing. *Proceedings of the National Academy of Sciences*, *121*(27), e2322163121. Retrieved from `https://www.pnas.org/doi/abs/10.1073/pnas.2322163121` doi: 10.1073/pnas.2322163121

Mazloff, M. R., Cornuelle, B., Gille, S. T., & Wang, J. (2020). The importance of remote forcing for regional modeling of internal waves. *Journal of Geophysical Research: Oceans*, *125*(2), e2019JC015623. doi: 10.1029/2019JC015623

Megann, A. (2018). Estimating the numerical diapycnal mixing in an eddy-permitting ocean model. *Ocean Modelling*, *121*, 19–33. doi: https://doi.org/10.1016/j.ocemod.2017.11.001

Megann, A., & Storkey, D. (2021). Exploring viscosity space in an eddy-permitting global ocean model: Is viscosity a useful control for numerical mixing? *Journal of Advances in Modeling Earth Systems*, *13*(5).

Melet, A., Nikurashin, M., Muller, C., Falahat, S., Nycander, J., Timko, P. G., ... Goff, J. A. (2013). Internal tide generation by abyssal hills using analytical theory. *Journal of Geophysical Research: Oceans*, *118*(11), 6303–6318.

Molemaker, M. J., McWilliams, J. C., & Dewar, W. K. (2015). Submesoscale instability and generation of mesoscale anticyclones near a separation of the California Undercurrent. *J. Phys. Oceanogr.*, *45*(3), 613–629. doi: 10.1175/JPO-D-13-0225.1

Momeni, K., Ma, Y., Peltier, W. R., Menemenlis, D., Thakur, R., Pan, Y., ... Alford, M. H. (2024). Breaking internal waves and ocean diapycnal diffusivity in a high-resolution regional ocean model: Evidence of a wave-turbulence cascade. *Journal of Geophysical Research: Oceans*, *129*(6), e2023JC020509. Retrieved from `https://agupubs.onlinelibrary.wiley.com/doi/abs/10.1029/2023JC020509` (e2023JC020509 2023JC020509) doi: https://doi.org/10.1029/2023JC020509

Munk, W., & Wunsch, C. (1998). Abyssal recipes II: Energetics of tidal and wind mixing. *Deep Sea Research Part I: Oceanographic Research Papers*, *45*(12), 1977–2010.

Naveira Garabato, A. C., Frajka-Williams, E. E., Spingys, C. P., Legg, S., Polzin, K. L., Forryan, A., ... Meredith, M. P. (2019). Rapid mixing and exchange of deep-ocean waters in an abyssal boundary current. *Proceedings of the National Academy of Sciences*, *116*(27), 13233–13238. Retrieved from `https://www.pnas.org/content/116/27/13233` doi: 10.1073/pnas.1904087116

Naveira Garabato, A. C., Polzin, K. L., King, B. A., Heywood, K. J., & Visbeck, M. (2004). Widespread intense turbulent mixing in the Southern Ocean. *Science*, *303*(5655), 210–213.

Nelson, A. D., Arbic, B. K., Menemenlis, D., Peltier, W. R., Alford, M. H., Grisouard, N., & Klymak, J. M. (2020). Improved internal wave spectral continuum in a regional ocean model. *Journal of Geophysical Research: Oceans*, *125*(5), e2019JC015974. Retrieved from `https://agupubs.onlinelibrary.wiley.com/doi/abs/10.1029/2019JC015974` (e2019JC015974 10.1029/2019JC015974) doi: https://doi.org/10.1029/2019JC015974

Olbers, D., & Eden, C. (2013). A global model for the diapycnal diffusivity induced by internal gravity waves. *Journal of Physical Oceanography*, *43*(8), 1759–1779.

Osborn, T. R. (1980). Estimates of the local rate of vertical diffusion from dissipation measurements. *Journal of physical oceanography*, *10*(1), 83–89.

Penven, P., Echevin, V., Pasapera, J., Colas, F., & Tam, J. (2005). Average circulation, seasonal cycle, and mesoscale dynamics of the Peru Current System: A modeling approach. *J. Geophys. Res.*, *110*(C10), C10021. doi: 10.1029/2005JC002945

Piron, A., Thierry, V., Mercier, H., & Caniaux, G. (2017). Gyre-scale deep convection in the subpolar north atlantic ocean during winter 2014–2015. *Geophysical Research Letters*, *44*(3), 1439–1447. doi: https://doi.org/10.1002/2016GL071895

Ruan, X., & Ferrari, R. (2021). Diagnosing diapycnal mixing from passive tracers. *Journal of Physical Oceanography*, *51*(3), 757–767. doi: https://doi.org/10.1175/JPO-D-20-0194.1

Saha, S., Moorthi, S., Pan, H.-L., Wu, X., Wang, J., Nadiga, S., … others (2010). The ncep climate forecast system reanalysis. *Bulletin of the American Meteorological Society*, *91*(8), 1015–1058. doi: https://doi.org/10.1175/2010BAMS3001.1

Samelson, R., & Vallis, G. K. (1997). Large-scale circulation with small diapycnal diffusion: The two-thermocline limit. *Journal of Marine Research*, *55*(2), 223–275.

Schifano, N. (2025). *Python codes and diffusivities extracted for all configurations of this article. zenodo.* Zenodo. Retrieved from `https://doi.org/10.5281/zenodo.15496614`

Shchepetkin, A. F. (2015). An adaptive, courant-number-dependent implicit scheme for vertical advection in oceanic modeling. *Ocean Modelling*, *91*, 38–69.

Shchepetkin, A. F., & McWilliams, J. C. (1998). Quasi-monotone advection schemes based on explicit locally adaptive dissipation. *Monthly Weather Review*, *126*(6), 1541–1580.

Shchepetkin, A. F., & McWilliams, J. C. (2003). A method for computing horizontal pressure-gradient force in an oceanic model with a nonaligned vertical coordinate. *Journal of Geophysical Research: Oceans*, *108*(C3). doi: 10.1029/2001JC001047

Shchepetkin, A. F., & McWilliams, J. C. (2005). The regional oceanic modeling system (roms): a split-explicit, free-surface, topography-following-coordinate oceanic model. *Ocean Modelling*, *9*(4), 347-404. Retrieved from `https://www.sciencedirect.com/science/article/pii/S1463500304000484` doi: https://doi.org/10.1016/j.ocemod.2004.08.002

Shchepetkin, A. F., & McWilliams, J. C. (2011). Accurate Boussinesq modeling with a practical, "stiffened"' equation of state. , *34*, 41-70.

Soufflet, Y., Marchesiello, P., Lemarié, F., Jouanno, J., Capet, X., Debreu, L., & Benshila, R. (2016). On effective resolution in ocean models. *Ocean Modelling*, *98*, 36–50. doi: https://doi.org/10.1016/j.ocemod.2015.12.004

Stommel, H. (1958). The abyssal circulation. *Deep-Sea Research*, *5*(1), 80-82. Retrieved from `https://www.sciencedirect.com/science/article/pii/S0146629158800144` doi: https://doi.org/10.1016/S0146-6291(58)80014-4

Taylor, G. (1922). Diffusion by continuous movements. *Proc. London Math. Soc.*, *2*(1), 196–212.

Thakur, R., Arbic, B. K., Menemenlis, D., Momeni, K., Pan, Y., Peltier, W. R., … Ma, Y. (2022). Impact of vertical mixing parameterizations on internal gravity wave spectra in regional ocean models. *Geophysical Research Letters*, *49*(16), e2022GL099614. doi: https://doi.org/10.1029/2022GL099614

Tozer, B., Sandwell, D. T., Smith, W. H. F., Olson, C., Beale, J. R., & Wessel, P. (2019). Global bathymetry and topography at 15 arc sec: Srtm15+. *Earth and Space Science*, *6*(10), 1847-1864. Retrieved from `https://agupubs.onlinelibrary.wiley.com/doi/abs/10.1029/2019EA000658` doi: https://doi.org/10.1029/2019EA000658

Version of the croco code used. (2025). Zenodo. Retrieved from `https://doi.org/10.5281/zenodo.15496859`

Vic, C., Ferron, B., Thierry, V., Mercier, H., & Lherminier, P. (2021). Tidal and near-inertial internal waves over the Reykjanes Ridge. *Journal of Physical Oceanography*, *51*, 419–437. doi: 10.1175/JPO-D-20-0097.1

Vic, C., Gula, J., Roullet, G., & Pradillon, F. (2018). Dispersion of deep-sea hydrothermal vent effluents and larvae by submesoscale and tidal currents. *Deep-Sea Research Part I*, *133*, 1–18. doi: 10.1016/j.dsr.2018.01.001

Waterhouse, A. F., MacKinnon, J. A., Nash, J. D., Alford, M. H., Kunze, E., Simmons, H. L., ... others (2014). Global patterns of diapycnal mixing from measurements of the turbulent dissipation rate. *Journal of Physical Oceanography*, *44*(7), 1854–1872. doi: https://doi.org/10.1175/JPO-D-13-0104.1

Wenegrat, J. O., Callies, J., & Thomas, L. N. (2018). Submesoscale baroclinic instability in the bottom boundary layer. *J. Phys. Oceanogr.*, *48*(11), 2571–2592. doi: 10.1175/JPO-D-17-0264.1

Whalen, C. B., de Lavergne, C., Naveira Garabato, A. C., Klymak, J. M., MacKinnon, J. A., & Sheen, K. L. (2020). Internal wave-driven mixing: governing processes and consequences for climate. *Nature Reviews Earth & Environment*, *1*(11), 606–621. Retrieved from `https://doi.org/10.1038/s43017-020-0097-z` doi: 10.1038/s43017-020-0097-z

Wise, A., Harle, J., Bruciaferri, D., O'Dea, E., & Polton, J. (2022). The effect of vertical coordinates on the accuracy of a shelf sea model. *Ocean Modelling*, *170*, 101935.

Zilberman, N., Becker, J., Merrifield, M., & Carter, G. (2009). Model estimates of M_2 internal tide generation over Mid-Atlantic Ridge topography. *Journal of Physical Oceanography*, *39*(10), 2635–2651. doi: 10.1175/2008JPO4136.1